Chemical Science

ROYAL SOCIETY OF CHEMISTRY

EDGE ARTICLE

View Article Online
View Journal

Open Access Article. Published on 09 March 2026. Downloaded on 3/10/2026 10:21:03 PM.
This article is licensed under a Creative Commons Attribution-NonCommercial 3.0 Unported Licence.

Check for updates

Cite this: DOI: 10.1039/d6sc01311b

All publication charges for this article have been paid for by the Royal Society of Chemistry

Red-light photoredox catalysis with bridged fluorescein derivatives: mechanistic insights and application to fluoride-responsive photopolymerization

Dokyeong Lee,[a] Hoyun Kim,[a] Byunghyuck Jung,[b] Sung Ho Yang,[c] Hong-In Lee *[a] and Jungkyu K. Lee *[a]

We demonstrated bridged fluoresceins (BFLs) as a class of metal-free red-light photocatalysts that feature structurally tunable and switchable activity in aqueous solutions. Mechanistic studies using photoinitiated radical polymerizations under controlled atmospheres revealed that BFLs engage in efficient oxidative and reductive quenching cycles with co-initiators proceeding through excitation, intersystem crossing, single-electron transfer, and regeneration processes. Notably, molecular oxygen plays dual roles: (i) serving as a co-initiator through O_2-derived reactive oxygen species that initiate radical chains, and (ii) functioning as a redox mediator that accelerates regeneration of BFL radical ions. Regarding the structure-performance relationship, bromine substituents on the BFL backbone considerably enhance photocatalytic efficacy by increasing spin–orbit coupling (*i.e.*, the heavy-atom effect), thereby promoting intersystem crossing yield. These findings are supported by thermodynamic and kinetic analyses, including voltammetry, time-resolved photoluminescence under cryogenic conditions, electron paramagnetic resonance (EPR) spectroscopy, and photobleaching studies. We also developed a switchable photoredox catalyst based on a sulfonyl-protected bridged fluorescein. This latent photocatalyst is selectively activated by fluoride ions to restore its photocatalytic activity, enabling red-light photopolymerization. Thus, this work not only offers fundamental mechanistic insights into photoredox catalysis and photoinitiated polymerization, but also establishes design principles for the development of switchable photocatalysts.

Received 13th February 2026
Accepted 2nd March 2026

DOI: 10.1039/d6sc01311b

rsc.li/chemical-science

Introduction

Inspired by nature, visible-light photoredox catalysis has attracted significant attention as a powerful strategy for driving chemical transformations under mild conditions, in which photoinduced electron-transfer processes generate reactive open-shell species that enable diverse reactions and applications.[1–8] However, most reported studies still rely on blue-to-green light (approximately 400–570 nm) to drive these reactions. Such relatively short wavelengths present several limitations, including potential safety risks, poor light penetration, susceptibility to photodegradation, and absorption overlap with common chromophores.[9] For example, exposure to blue light can increase the risk of retinal photodamage and fails to penetrate the dermal layer of skin, thereby restricting access to biological targets.[10,11] These limitations motivate the development of photocatalysis that operates efficiently at longer wavelengths, offering safer and more versatile platforms for photochemical and photobiological applications.

Red-light photoredox catalysis provides distinct advantages, including lower energy requirements, reduced phototoxicity, and deeper penetration, rendering it highly attractive for a wide range of applications.[12–16] The lower photon energy can also enable enhanced selectivity. For example, Gianetti and co-workers demonstrated that red light selectively activates weaker bonds such as C(sp^2)-I, facilitating chromoselective catalysis, whereas blue light activates stronger C(sp^2)-Br bonds.[17] Furthermore, MacMillan and co-workers demonstrated a compelling biological application: proximity-based mapping of complex biological environments. This microenvironment mapping strategy highlighted the ability of red light to minimize health risks and penetrate deeply into tissue, thus enabling biological and *in vivo* applications.[18] In addition, Matyjaszewski and co-workers synthesized well-defined polymers under biologically relevant conditions through red-light-induced atom transfer radical polymerization.[19,20]

[a]Department of Chemistry and Green-Nano Materials Research Center, Kyungpook National University, Daegu 41566, South Korea. E-mail: jkl@knu.ac.kr; leehi@knu.ac.kr

[b]Department of Physics and Chemistry, Daegu Gyeongbuk Institute of Science and Technology (DGIST), Daegu 42988, South Korea

[c]Department of Chemistry Education, Korea National University of Education, Cheongju 28173, South Korea

Open Access Article. Published on 09 March 2026. Downloaded on 3/10/2026 10:21:03 PM.
This article is licensed under a Creative Commons Attribution-NonCommercial 3.0 Unported Licence.

Despite these benefits, the intrinsically lower photon energy of red light presents fundamental challenges in reactivity, emphasizing the critical need for more efficient photocatalysts.[21] Additionally, metal-free red-light photoredox catalysts have emerged as a promising class of materials, featuring finely tunable redox potentials that enable broad substrate compatibility and low cytotoxicity for biological applications.[22,23] For example, methylene blue is widely employed as a red-light photoredox catalyst due to its high photoredox catalytic efficiency.[24–26] However, structural modification through chemical functionalization remains challenging, thereby limiting opportunities for further development. In particular, incorporating stimulus-responsive functionalities could further expand the versatility of photocatalysts for advanced applications, including polymerization-based signal amplification, cell encapsulation, and photodynamic therapy.

Fluorescein derivatives are widely utilized as representative organic photocatalysts in green-light photoredox catalysis, exhibiting robust performance under aerobic conditions with both electron donors and electron acceptors.[27,28] Furthermore, their low cytotoxicity, good water solubility, high accessibility, and ease of structural modification make them highly attractive for expanding their application scope.[29] For example, we previously demonstrated their successful use in selective hydrogelation, enabling both single-cell nanoencapsulation and naked-eye detection of target analytes *via* photoinitiated polymerization.[30–33] Recently, bridged fluorescein derivatives (BFLs) were shown to catalyze the C–H arylation of (hetero) arenes with diazonium salts under red-light irradiation and inert atmosphere conditions.[34,35]

Owing to their facile synthetic accessibility to diverse structural derivatives and favorable water solubility, BFLs were selected in this work as red-light photoredox catalysts to elucidate the underlying catalytic mechanisms under different atmospheric conditions. Three different BFLs were synthesized, and their photocatalytic activities were systematically evaluated through photoinitiated radical polymerizations, which offer a convenient platform for assessing catalytic performance due to their rapid kinetics and straightforward characterization.[27,36] In particular, photoinduced reversible addition–fragmentation chain transfer (photo-RAFT) polymerization as a controlled/living radical polymerization (CRP) and photoinduced free-radical polymerization were employed to investigate mechanistic insights under different atmospheric environments (Fig. 1). In free-radical photopolymerization, the reductive and oxidative quenching cycles were thoroughly investigated as the primary photoredox pathways. Finally, we demonstrated stimuli-responsive red-light photoredox catalysis using a fluoride ion-responsive photocatalyst through free-radical photopolymerization, highlighting its potential for advanced photopolymerization applications.

Results and discussion

Synthesis and characterization of bridged fluorescein derivatives (BFLs)

BFLs were readily synthesized from fluorescein derivatives through Friedel–Crafts cyclization in the presence of sulfuric acid, as described in the literature.[34,35] Typically, fluorescein analogue was dissolved in concentrated sulfuric acid and stirred at 180 °C for 24 h under an argon atmosphere. After the purification processes, the yields of black solids were 31.7% for bridged fluorescein (coerulein B, or **CB**), 52.2% for bridged dibromofluorescein (**BBF**), and 45.9% for bridged eosin Y (**BEY**), as detailed in the SI. For example, we suggest the following mechanism for **BEY**: initial protonation of carbonyl oxygen by a Brønsted–Lowry acid activates it toward electrophilic aromatic substitution with the adjacent aromatic ring, yielding a sigma complex bearing a diol group. Subsequent deprotonation restores aromaticity, and further protonation of the diol leads to water elimination *via* an oxonium ion intermediate. This step is followed by an oxa-Michael addition,[37] accompanied by elimination of a bromide ion, resulting in formation of the new carbonyl oxygen (Scheme S1).

The obtained BFLs were initially characterized using NMR and mass spectrometry (Fig. S1–S8). Additionally, UV-vis and

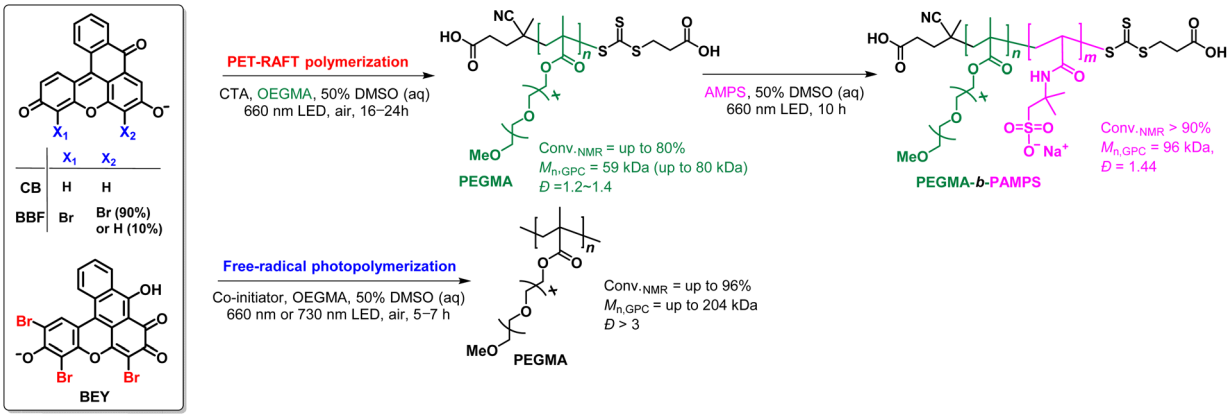

Fig. 1 Schematic depiction of photo-RAFT and free-radical photopolymerization using BFLs under irradiation of red light. **CB**: coerulein B; **BBF**: bridged dibromofluorescein; **BEY**: bridged eosin Y; CTA: chain-transfer agent; OEGMA: oligo(ethylene glycol) methyl ether methacrylate; AMPS: 2-acrylamido-2-methyl-1-propanesulfonate.

 © 2026 The Author(s). Published by the Royal Society of Chemistry

Open Access Article. Published on 09 March 2026. Downloaded on 3/10/2026 10:21:03 PM.
This article is licensed under a Creative Commons Attribution-NonCommercial 3.0 Unported Licence.

fluorescence spectra of the BFLs showed excitation and emission in the 600–800 nm range (Fig. S9). The wavelengths of maximum visible excitation ($\lambda_{ex,vis}$) and their corresponding molar absorptivity (ε) were 600 nm ($\varepsilon = 1225$ cm^{-1} M^{-1}) for **CB**, 605 nm ($\varepsilon = 1385$ cm^{-1} M^{-1}) for **BBF**, and 620 nm ($\varepsilon = 1340$ cm^{-1} M^{-1}) for **BEY**. This trend exhibits a red shift in λ_{ex} with increasing numbers of incorporated bromine atoms, presumably due to the heavy halogen atom effect.[38,39] Furthermore, the wavelengths of maximum fluorescence (λ_f) were 740 nm for **CB**, 770 nm (with a shoulder at 720 nm) for **BBF**, and 740 nm for **BEY**.

Photo-RAFT polymerization

We carried out this CRP using BFLs as red-light photoredox catalysts/initiators under various reaction conditions to elucidate the mechanisms of photoredox catalysis and photopolymerization. In addition, three different BFLs (**CB**, **BBF** and **BEY**) were systematically evaluated to correlate molecular structure with photocatalytic performance. Oligo(ethylene glycol) methyl ether methacrylate (OEGMA) was used as a water-soluble and biocompatible monomer, while 4-((((2-carboxyethyl)thio)carbonothioyl)thio)-4-cyanopentanoic acid (**1**) served as a water-soluble RAFT chain transfer agent (CTA) exhibiting high compatibility with methacrylates.[40] A red light-emitting diode (LED) (660 ± 30 nm, 5.9 W cm^{-2}) was used as the red-light source.

Kinetic investigations were conducted using ^{1}H NMR spectroscopy and GPC analysis to monitor the evolution of the number-average molecular weight (M_n) and dispersity ($Đ$) as functions of monomer conversion under various reaction conditions. To ensure accurate determination of monomer conversion by ^{1}H NMR, dimethylmalonic acid was chosen as an internal standard because the intense signal of the ethylene glycol unit partially overlaps with the characteristic methoxy peak of OEGMA.[41] Overall, the results demonstrated that both monomer conversion and $\ln([M]_0/[M]_t)$ increased linearly with irradiation time, indicating a controlled radical polymerization process. In addition, a linear relationship was observed between the experimentally determined molecular weight ($M_{n,exp}$ from GPC) and monomer conversion. Furthermore, GPC analysis revealed consistently narrow $Đ$ values throughout the polymerization, and the progressive shift of the monomodal GPC traces toward the high molecular weights provided additional evidence for the controlled/living nature of the polymerization.

Typically, photo-RAFT polymerization was performed in an NMR tube containing a 50% DMSO (aq) solution of each BFL (0.1 mM), OEGMA (250 mM), and CTA (**1**) (1.25 mM) under red-light irradiation for 24 h (Table 1, entries 1–3). As a result, **BEY**

Table 1 Photo-RAFT polymerization of OEGMA with different BFLs under various reaction conditions using red LED light (660 ± 30 nm, 5.9 W cm^{-2}) irradiation[a]

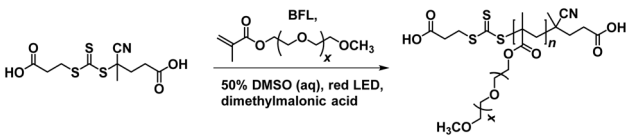

Entry	Type of BFL	[OEGMA] : [CTA] : [TEOA] : [BFL](mM)	Conv.[b] (%)	$M_{n,theo}$[c] (kDa)	$M_{n,exp}$[d] (kDa)	$Đ$[d]	Atm.
1	**CB**	250 : 1.25 : 0 : 0.1	<1	<1	<1	n.a.	Air
2	**BBF**	250 : 1.25 : 0 : 0.1	57	57	37	1.36	Air
3	**BEY**	250 : 1.25 : 0 : 0.1	80	80	80	1.33	Air
4	**BEY**	250 : 2.50 : 0 : 0.1	60	30	27	1.24	Air
5	**BEY**	250 : 5.00 : 0 : 0.1	34	8	8	1.23	Air
6	**CB**	250 : 1.25 : 1 : 0.1	<1	<1	<1	n.a.	Air
7	**BBF**	250 : 1.25 : 1 : 0.1	25	25	30	1.35	Air
8	**BEY**	250 : 1.25 : 1 : 0.1	77	77	58	1.35	Air
9	**BEY**	250 : 1.25 : 3 : 0.1	73	73	57	1.42	Air
10	**BEY**	250 : 1.25 : 5 : 0.1	65	65	51	1.46	Air
11	**BEY**	250 : 2.50 : 1:0.1	9	5	8	1.27	Air
12	**BEY**	250 : 0 : 1 : 0.1	95	n.a.	≥767[e]	3–4	Air
13	none	250 : 1.25 : 1 : 0	<1	<1	<1	n.a.	Air
14	**BEY**	250 : 0 : 0 : 0.1	77	n.a.	≥767[e]	3–4	Air
15	**BEY**	250 : 0 : 0 : 0.1	3	n.a.	<1	n.a.	Ar[f]
16	**BEY**	250 : 0 : 0 : 0.1	86	n.a.	≥767[e]	3–4	O_2[f]
17	**BEY**	250 : 1.25 : 0 : 0.1	68	68	63	1.31	Ar[f]
18	**BEY**	250 : 1.25 : 0 : 0.1	85	85	85	1.34	O_2[f]

[a] Photopolymerization was typically conducted in a standard NMR tube sealed with a cap, containing 0.6 mL of a 1 : 1 (v/v) mixture of DMSO and D_2O under aerobic conditions at room temperature for 24 h. [b] Monomer conversion (%) was determined by ^{1}H NMR using dimethylmalonic acid as an internal standard, as detailed in the SI. [c] Theoretical molecular weight ($M_{n,theo}$) was determined using the equation: $M_{n,theo} = ([OEGMA]_0 - [OEGMA]_t)/[CTA]_0 \times M_{OEGMA} + M_{CTA}$. [d] Experimental molecular weights and polydispersity ($Đ$) were determined by GPC analysis using PMMA standards for calibration with DMF, containing 1 mM LiBr, as the luent as detailed in the SI. [e] The upper detection limit. [f] A J-Young NMR tube equipped with a valve was used for reactions under Ar (g) and O_2 (g) atmospheres. TEOA: triethanolamine, n.a.: not applicable.

Open Access Article. Published on 09 March 2026. Downloaded on 3/10/2026 10:21:03 PM.
This article is licensed under a Creative Commons Attribution-NonCommercial 3.0 Unported Licence.

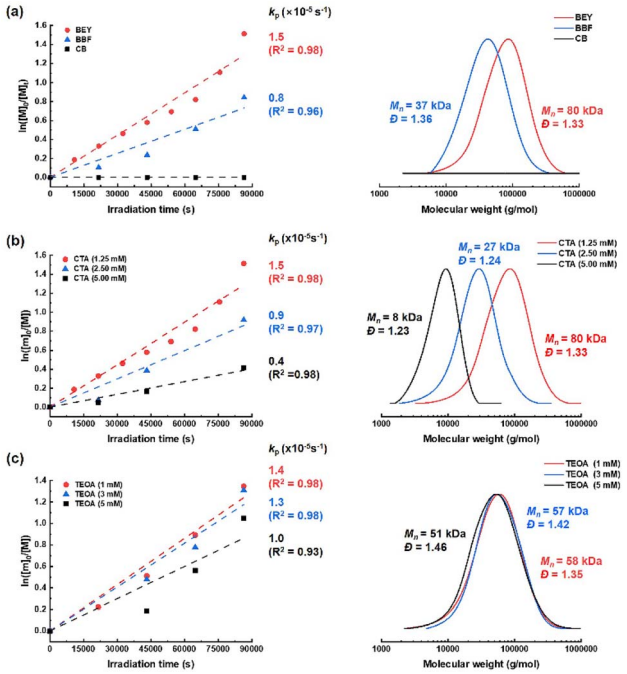

Fig. 2 Polymerization kinetics of OEGMA (left) and corresponding GPC traces (right) under various reaction conditions: (a) different BFL types, (b) varying concentrations of CTA (**1**) with **BEY**, and (c) varying concentrations of TEOA with **BEY**.

exhibited superior vinyl conversion of up to 80% with a first-order rate coefficient ($k_p = 1.5 \times 10^{-5}$ s^{-1}), yielding a polymer (PEGMA) with $M_n = 80$ kDa ($Đ = 1.33$) (Fig. 2a). However, the monomer conversion with **BBF** and **CB** afforded lower monomer conversions of 57% ($k_p = 0.8 \times 10^{-5}$ s^{-1}, $M_n = 37$ kDa, $Đ = 1.36$) and negligible conversion, respectively. As a control experiment, eosin Y (EY), as a representative non-bridged fluorescein, was employed to benchmark the photoredox catalytic performance against **BEY**. Under reaction conditions identical to those in Table 1, entry 3, EY exhibited no monomer conversion, whereas **BEY** afforded 60% monomer conversion after 18 h of irradiation. Upon extending the irradiation time to 24 h, EY achieved only 17% monomer conversion, while **BEY** reached 80% monomer conversion (Fig. S10).

Under the same reaction conditions as entry 3, increasing the CTA concentration to 5 mM led to a substantial decrease in monomer conversion to 34% ($k_p = 0.4 \times 10^{-5}$ s^{-1}) and a corresponding reduction in M_n to 8 kDa ($Đ = 1.23$) (Fig. 2b). This rate retardation is assumed to arise from cross-termination, which appears to be a dominant pathway in the RAFT process (Table 1, entries 4 and 5).[42] In the presence of triethanolamine (TEOA, 1 mM) as a co-initiator, monomer conversion further decreased for BFLs (Table 1, entries 6–8). For example, the conversions and corresponding M_n values were 77% ($k_p = 1.4 \times 10^{-5}$ s^{-1}, $M_n = 58$ kDa) for **BEY**, 25% ($k_p = 0.3 \times 10^{-5}$ s^{-1}, $M_n = 30$ kDa) for **BBF**, and negligible for **CB** (Fig. S11a). Notably, monomer conversions in the presence of TEOA were consistently lower than that those observed in its absence.

These results were further supported by experiments using **BEY**, where increasing TEOA concentration from 1 mM to 5 mM decreased the monomer conversion from 77% to 65% and reduced M_n from 58 kDa to 51 kDa (Table 1, entries 8–10) (Fig. 2c). In addition, the experimentally observed M_n values were lower than the theoretical M_n values. We attribute this deviation to the increased concentration of TEOA radical cation species, which disrupts the RAFT equilibrium of the CTA.[43] Furthermore, this retardation became even more pronounced when the concentration of CTA (**1**) was increased to 2.5 mM in the presence of TEOA (1 mM). As a result, the monomer conversion was only 9% ($k_p = 0.1 \times 10^{-5}$ s^{-1}), yielding a corresponding M_n of 8 kDa (Table 1, entry 11) (Fig. S11b). However, in the absence of the CTA, the monomer conversion reached 95%, affording a polymer with M_n exceeding 767 kDa, indicative of a free-radical polymerization process (Table 1, entry 12) (Fig. S12). Furthermore, no monomer conversion was observed in the absence of **BEY** (Table 1, entry 13), confirming that CTA (**1**) does not act as a photoiniferter under these reaction conditions (Fig. S12).

Based on these results, we propose a mechanism that excludes the participation of molecular oxygen (O_2) as illustrated in Fig. 3a. Upon exposure to red light, BFL is excited to its singlet-excited state and then transitions to the triplet-excited state (^{3}BFL*) *via* intersystem crossing (ISC). In the absence of TEOA, ^{3}BFL* either reduces CTA through a single-electron transfer (SET) process, generating CTA radical anion (CTA$^{\cdot-}$) (Fig. 3a, highlighted in red).[43] This photoinduced electron transfer (PET) process is thermodynamically favorable, as evidenced by the Gibbs free energy change ($\Delta G_{PET} = -0.4$ to -0.43 eV) determined from electrochemical measurements and time-resolved photoluminescence spectroscopy (discussed in detail in the section below). The CTA radical anion subsequently undergoes fragmentation through a dissociative electron transfer process, generating a propagating radical species and a thiocarbonylthio anion. These radical intermediates then participate in the RAFT process involving reversible chain-transfer equilibria that facilitate redistribution among propagating chains during polymerization (Fig. 3a, highlighted in green).[44] Subsequently, the formed BFL radical cation (BFL$^{\cdot+}$) is regenerated to BFL through a SET process with the CTA radical anion.

In the presence TEOA, ^{3}BFL* oxidizes TEOA through a SET process, producing BFL radical anion (BFL$^{\cdot-}$) and TEOA radical cation (TEOA$^{\cdot+}$). This process is supported by the negative ΔG_{PET} values (-0.25 to -0.31 eV). The BFL radical anion subsequently undergoes the dissociative process, generating a propagating radical that initiates the RAFT polymerization. Conversely, the CTA radical anion is rapidly converted into an inert form through a SET process with the TEOA radical cation (Fig. 3a, highlighted in blue).[45] This quenching pathway involving TEOA disrupts propagation of the RAFT polymerization, resulting in the observed decreases in both polymerization rate and M_n.

In the absence of both CTA (**1**) and TEOA, the photoreaction of OEGMA with **BEY** was conducted under different atmospheres (Table 1, entries 14–16). Under ambient atmosphere, the monomer conversion reached 77%, and M_n exceeded the detecting limit ($Đ = 3$–4) after 24 h of irradiation (Fig. 4a).

 © 2026 The Author(s). Published by the Royal Society of Chemistry

Open Access Article. Published on 09 March 2026. Downloaded on 3/10/2026 10:21:03 PM.
This article is licensed under a Creative Commons Attribution-NonCommercial 3.0 Unported Licence.

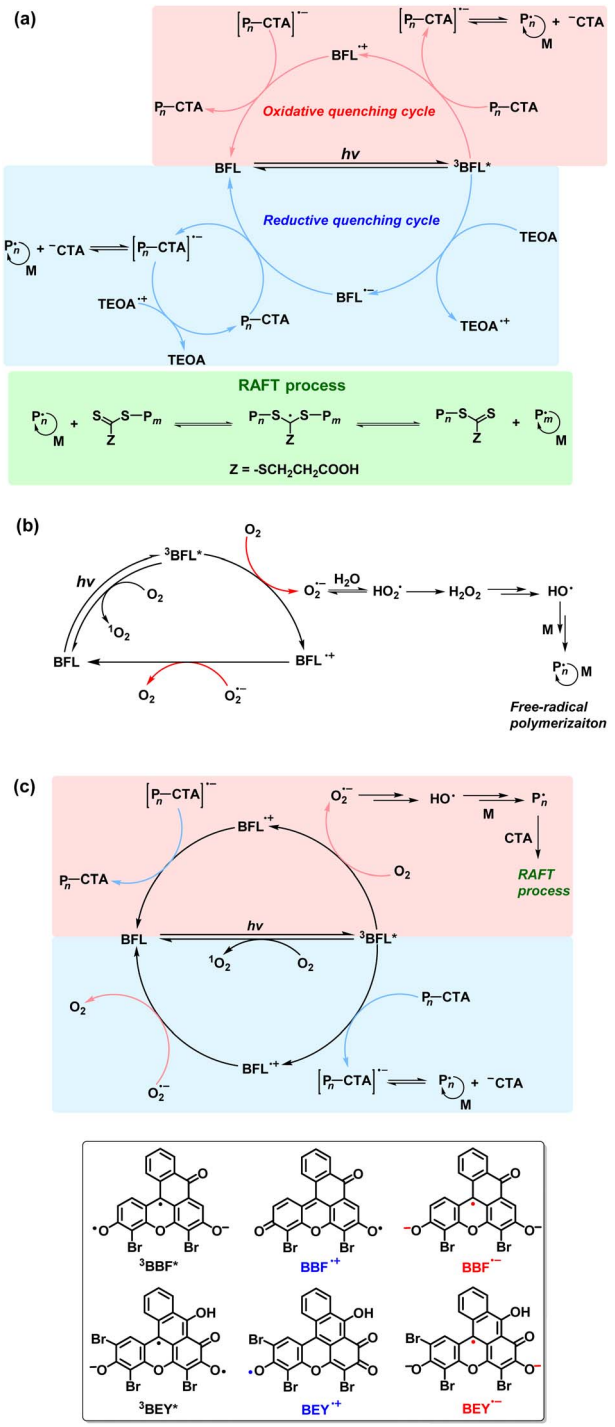

Fig. 3 Plausible mechanisms using BFLs for (a) oxidative photo-RAFT polymerization in the absence of O_2 (top) and reductive photo-RAFT (bottom) with TEOA in the absence of O_2, (b) photoinduced free-radical polymerization with O_2 in the absence of both CTA and TEOA, and (c) photoinduced oxidative electron-transfer RAFT polymerization in the presence of O_2.

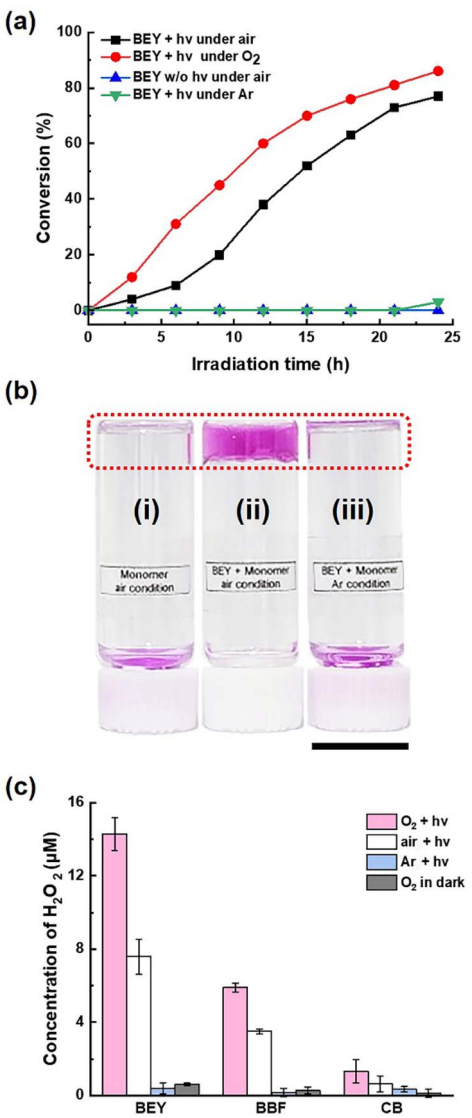

Fig. 4 (a) Monomer conversion in the absence of both CTA (**1**) and TEOA under different atmospheric conditions, (b) representative images of photopolymerization conducted under (i) monomer only in an ambient atmosphere, (ii) **BEY** with monomer in an ambient atmosphere, and (iii) **BEY** with monomer in an argon atmosphere, and (c) quantitative analysis of hydrogen peroxide generated by BFLs. The scale bar represents 1.5 cm.

Notably, even 50% monomer conversion was sufficient to form a hydrogel. However, when the photopolymerization was performed in a J-Young NMR tube under an argon atmosphere under otherwise identical conditions, only 3% monomer conversion was observed after 24 h of irradiation, and no hydrogel formation occurred (Table 1, entry 15). Hydrogel formation was further confirmed by a vial test (Fig. 4b). After 24 h of irradiation, a staining dye was added to visualize the hydrogel. Upon inversion, the red-stained hydrogel remained at the top, while the unreacted solution settled at the bottom. Thus, hydrogelation was observed under aerobic conditions (Fig. 4b, ii), whereas no hydrogelation occurred under an argon atmosphere (Fig. 4b, iii) or in the dark as a negative control. Remarkably, under an oxygen-rich atmosphere, the monomer conversion recovered to 86%, with M_n again exceeding the detection limit (Table 1, entry 16) (Fig. 4a). These results indicate that O_2 plays a crucial role in enabling the polymerization in the absence of co-initiators.

Open Access Article. Published on 09 March 2026. Downloaded on 3/10/2026 10:21:03 PM.
This article is licensed under a Creative Commons Attribution-NonCommercial 3.0 Unported Licence.

As a negative control, irradiation of the monomer only for 24 h resulted in neither monomer conversion nor hydrogel formation (Fig. 4b, i), confirming that **BEY** is essential for initiating the polymerization. Furthermore, in the presence of **BEY**, no monomer conversion was observed in the dark at either room temperature or 40 °C after 24 h, confirming that light is required to activate **BEY** and initiates the polymerization (Fig. S13).

In addition, given that DMSO can generate methyl radicals under photoredox conditions,[46,47] the photopolymerization of OEGMA using **BEY** was performed in pure water to evaluate the effect of DMSO (Fig. S14). Notably, the solubility of BFLs in pure water is limited, but is significantly improved upon addition of OEGMA. Under ambient conditions, the polymerization in water exhibited a prolonged induction period of up to 5 h. However, upon extending the irradiation time beyond 9 h, the monomer conversion in water exceeded that obtained in 50% DMSO (aq). After 24 h of irradiation, monomer conversions of 96% and 77% were achieved in water and 50% DMSO (aq), respectively. Under oxygen-rich conditions, the polymerization rates in both water and 50% DMSO (aq) increased, while the overall trend remained similar to those observed under ambient conditions. In contrast, under an argon atmosphere, no monomer conversion was observed up to 18 h in either solvent system. Consequently, these results indicate that oxygen plays a more critical role than DMSO in governing the photopolymerization behavior.

These observed results suggest a photoredox mechanism involving O_2 (Fig. 3b). ^{3}BFL* facilitates the reduction of O_2 through a SET process, producing superoxide ($O_2^{\cdot -}$) and BFL radical cation. Acting as a Brønsted–Lowry base, the superoxide ($pK_{aH} = 4.8$) can abstract a proton from weakly acidic substrates such as water to form the hydroperoxyl radical ($HO_2^{\cdot}$).[48] Thus, hydroperoxyl radical is then converted to hydrogen peroxide through reaction with either superoxide or another hydroperoxyl radical. We assume that the generated hydrogen peroxide can be activated by ^{3}BFL* to produce hydroxyl radical ($HO^{\cdot}$) (Fig. S15 and S16). The resulting hydroxyl radical initiates free-radical polymerization of OEGMA.[49,50] For example, Deng and co-workers demonstrated that red-light-induced photo-RAFT polymerization using methylene blue can be facilitated by hydroxyl radicals generated through a photo-Fenton-like process.[51,52] Meanwhile, the BFL radical cation is regenerated to BFL through a SET process with superoxide.

We confirmed the generation of hydrogen peroxide using a quantitative colorimetric assay based on peroxidase and *N*,*N*-diethyl-*p*-phenylenediamine sulfate (DPD).[53] This analysis was conducted with BFLs (0.1 mM) under different atmospheric conditions (detailed in the SI). The results showed that oxygen-rich conditions produced higher concentrations of hydrogen peroxide than other conditions (Fig. 4c and S17). For example, after 10 min of irradiation under an oxygen-rich atmosphere, the concentrations of hydrogen peroxide were 14 μM for **BEY**, 6 μM for **BBF**, and 2 μM for **CB**. Under an ambient atmosphere, these values decreased to 7 μM for **BEY**, 5 μM for **BBF**, and 1 μM for **CB**, while under an argon atmosphere hydrogen peroxide formation was negligible for all BFLs. As a control experiment, the generation of hydrogen peroxide was negligible for all BFLs in the dark, even under an oxygen-rich atmosphere. There results indicate that the generation of hydrogen peroxide is significantly influenced by both the O_2 concentration and the type of BFL.[54]

Additionally, photo-RAFT polymerization with **BEY** and CTA (**1**) was performed under different atmospheric conditions (Table 1, entries 3, 17, and 18) to elucidate the role of O_2 (Fig. 5). Under an argon atmosphere, the initial monomer conversion proceeded markedly slower than under aerobic atmospheres. For example, after 12 h, the monomer conversion was only 10% ($k_p = 0.2 \times 10^{-5}$ s^{-1}) under an argon atmosphere, whereas oxygen-rich and ambient atmospheres yielded 56% ($k_p = 1.9 \times 10^{-5}$ s^{-1}) and 40% ($k_p = 1.4 \times 10^{-5}$ s^{-1}) conversion, respectively. Despite these differences in polymerization rate, the photopolymerizations exhibited characteristic of CRP under all atmospheric conditions. A linear increase in M_n with monomer conversion, accompanied by progressive narrowing of the molecular weight distribution, confirmed the controlled nature of the process. For example, after 24 h of irradiation, 85% monomer conversion under oxygen-rich conditions yielded 85 kDa of M_n ($Đ = 1.34$), while 68% monomer conversion under argon resulted in $M_n = 63$ kDa ($Đ = 1.31$). These results indicate that O_2 facilitates RAFT polymerization, presumably by acting as both a reductant for the **BEY** radical cation and a co-initiator. We assume that the superoxide regenerates **BEY** from its cation radical species through a SET process, thereby enhancing catalytic performance (Fig. 3c). Furthermore, hydroxyl radicals generated from superoxide-derived intermediates, initiate the radical reaction. During initiation, oligomeric radicals are formed, which subsequently react with the CTA and propagate through the RAFT process, leading to CRP.

We also applied this methodology to chain-extension polymerization, further confirming that the process proceeds through the RAFT mechanism. For instance, photopolymerization was carried out in a vial containing 50% DMSO (aq) with **BEY** (0.3 mM), OEGMA (200 mM), CTA (**1**) (1.25 mM) under ambient conditions under red-light irradiation. After 16 h, monomer conversion exceeded 90%, yielding M_n of 59 kDa ($Đ = 1.36$). The synthesized PEGMA was characterized by ^{1}H NMR and GPC profile. For example, the characteristic OEGMA peaks at 6.0, 5.7 and 4.2 ppm nearly disappeared (Fig. 6a, highlighted in pink), while broad peaks at 4.0 ppm and 0.9 ppm emerged (highlighted with asterisks), indicating successful formation of PEGMA. Furthermore, GPC analysis revealed a monomodal trace with a narrow molecular weight distribution (Fig. 6b). The resulting solution was then directly added with 2-acrylamido-2-methyl-1-propanesulfonate (AMPS, 250 mM) without an isolation step.

After 10 h, ^{1}H NMR analysis revealed the monomer conversion exceeding 90%. The characteristic peaks of AMPS at 5.5, 6.0 and 6.2 ppm disappeared, while broad peaks at 3.4 and 2.0 ppm appeared, confirming formation of PEGMA-*b*-poly(AMPS). Additionally, the shift of the monomodal GPC trace toward higher molecular weight further confirmed formation of the diblock copolymer, PEGMA-*b*-poly(AMPS). This successful chain extension demonstrates excellent retention of chain-end group

 © 2026 The Author(s). Published by the Royal Society of Chemistry

Open Access Article. Published on 09 March 2026. Downloaded on 3/10/2026 10:21:03 PM.
This article is licensed under a Creative Commons Attribution-NonCommercial 3.0 Unported Licence.

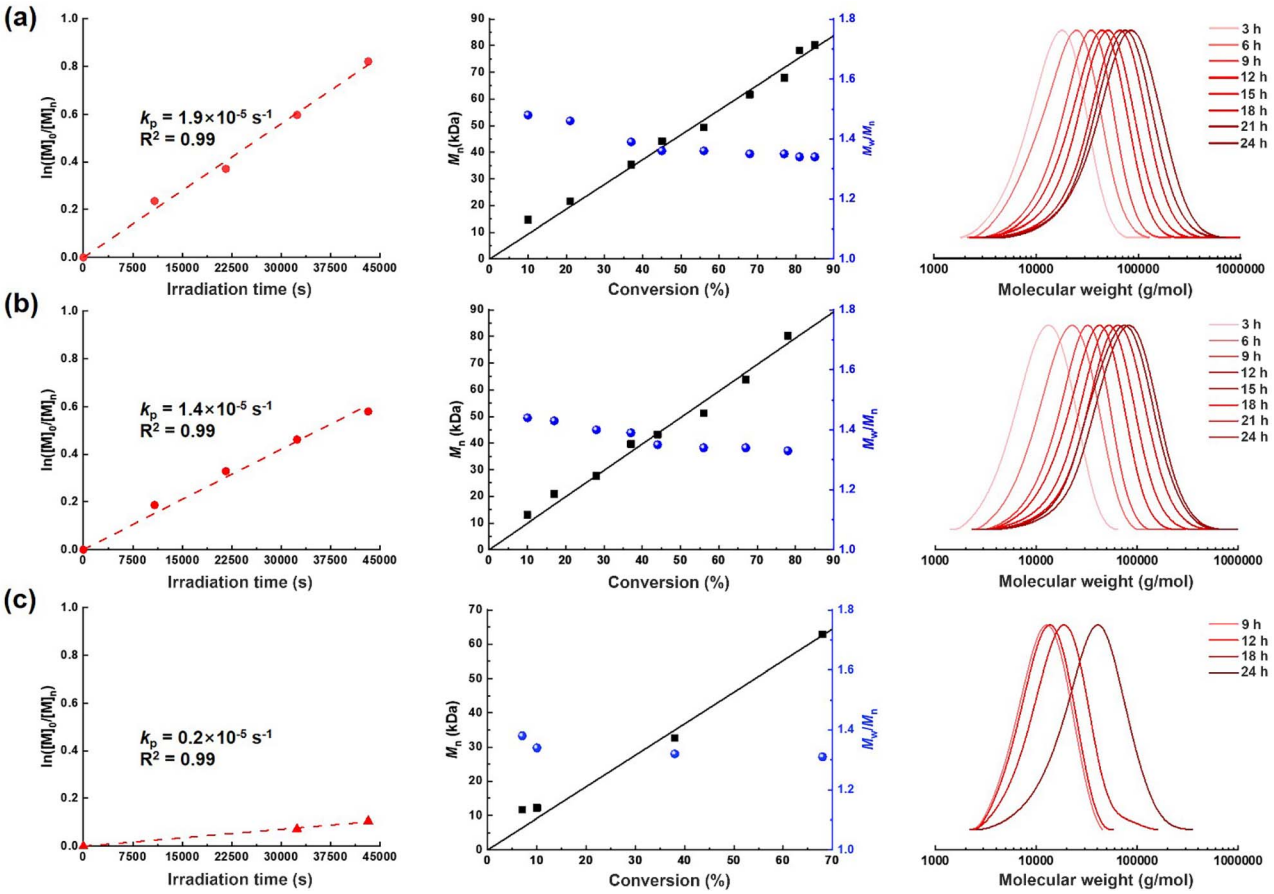

Fig. 5 Experimental results of photo-RAFT polymerization of OEGMA under different atmospheric conditions. Shown are (left) kinetic plots, (middle) evolution of M_n (squares) and dispersity (circles) as functions of monomer conversion, and (right) corresponding GPC traces for (a) oxygen-rich, (b) ambient, and (c) argon atmospheres.

fidelity. To evaluate temporal control, an on–off light experiment was conducted under the same conditions as Table 1, entry 3. The light was cycled on and off repeatedly until over 60% monomer conversion was achieved, with no detectable conversion during the dark intervals (Fig. 6c). This light-regulated temporal control confirms that polymerization can be precisely controlled through light-mediated activation and deactivation.

Free-radical photopolymerization

The photoinitiated free-radical polymerization of OEGMA (250 mM) with BFLs was investigated under various reaction conditions. **BEY** exhibited superior performance compared to **BBF** and **CB**. For example, in the presence of TEOA (100 mM), **BEY** (0.01 mM) achieved 84% monomer conversion with an apparent first-order reaction rate ($k_{app} = 0.7 \times 10^{-5}$ s^{-1}), yielding PEGMA with $M_n = 114$ kDa ($Đ = 3.4$) after 5 h under ambient conditions (Fig. S18). In contrast, **BBF** and **CB** afforded monomer conversions of 77% ($k_{app} = 0.4 \times 10^{-5}$ s^{-1}) and 6% ($k_{app} = 0.1 \times 10^{-5}$ s^{-1}), respectively, affording M_n values of 56 kDa ($Đ = 3.2$) and 108 kDa ($Đ = 3.4$) under the same reaction conditions (Table 2, entries 1–3). As the concentration of BFLs increased, the polymerization rate increased accordingly. For instance, at 0.1 mM, **BEY** and **BBF** achieved monomer conversions of 96% ($k_{app} = 3.1 \times 10^{-4}$ s^{-1}) and 91% ($k_{app} = 1.6 \times 10^{-4}$ s^{-1}), respectively (Fig. S19). However, the corresponding M_n values decreased significantly to 24 kDa ($Đ = 2.6$) for **BEY** and 60 kDa ($Đ = 2.7$) for **BBF** (Table 2, entries 4 and 5). This decrease is attributed to the higher concentration of BFLs, which act as both photocatalysts and initiators, generating a greater number of radical intermediates that initiate more polymer chains, and thus reduce the average chain length. As negative controls, no monomer conversion was observed under the optimized reaction conditions in the dark after 24 h. Similarly, no monomer conversion was observed in the absence of BFLs after 24 h of irradiation (Table 2, entries 6 and 7) (Fig. S19). However, hydrogel formation was observed in the presence of monomer and **BEY** without TEOA, consistent with the previously described result (Table 1, entry 14).

The photopolymerization of OEGMA with **BEY** in the presence of TEOA was conducted under different atmospheric conditions (Table 2, entries 8 and 9). Under an argon atmosphere, the monomer conversion decreased by 23% compared to that under an ambient atmosphere, yielding 73% conversion ($k_{app} = 0.7 \times 10^{-4}$ s^{-1}) with M_n of 19 kDa ($Đ = 2.5$) after 5 h of irradiation (Fig. S20). In contrast, under an oxygen-rich

Open Access Article. Published on 09 March 2026. Downloaded on 3/10/2026 10:21:03 PM.
This article is licensed under a Creative Commons Attribution-NonCommercial 3.0 Unported Licence.

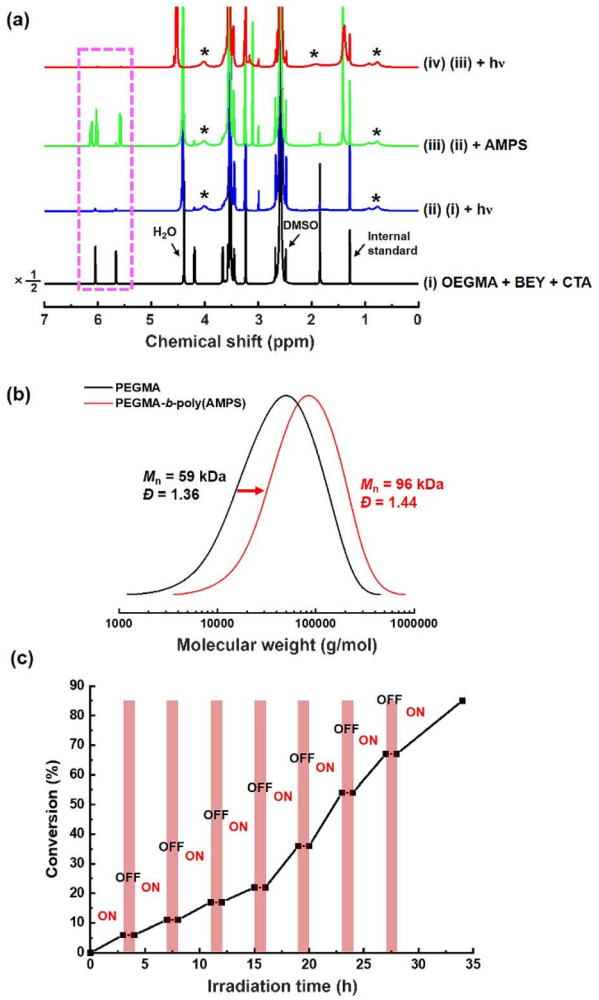

Fig. 6 (a) ^{1}H NMR spectra of stepwise diblock copolymerization of PEGMA-*b*-poly(AMPS), (b) the corresponding GPC traces, and (c) monomer conversion demonstrating light-regulated temporal control.

atmosphere, monomer conversion increased to 92% ($k_{app} = 1.9 \times 10^{-4}$ s^{-1}), yielding PEGMA with $M_n = 21$ kDa ($Đ = 2.4$). These results indicate that O_2 promotes this photopolymerization. We assume that O_2 facilitates continuous redox cycling of **BEY** by oxidizing the **BEY** radical anion through a SET process (Fig. 7). Notably, this effect depends on the concentration of O_2. Excessive amounts of O_2 reduce the polymerization rate relative to that observed under ambient conditions, presumably by suppressing the SET pathway between ^{3}**BEY*** and TEOA. Under these conditions, O_2 oxidizes ^{3}**BEY*** to produce **BEY** radical cation while simultaneously decreasing the concentration of α-amino radical species, thereby retarding polymerization. Furthermore, under near-infrared (NIR) irradiation, **BEY** achieved 93% monomer conversion ($k_{app} = 1.2 \times 10^{-4}$ s^{-1}) after 7 h, yielding PEGMA with M_n of 22 kDa ($Đ = 2.6$) under ambient conditions (Table 2, entry 10) (Fig. S21).

As control experiments, methylene blue and EY, were also employed to benchmark the photoredox catalytic performance against **BEY**. Under reaction conditions identical to those in Table 2, entry 5, EY exhibited an induction period of approximately 1 h and achieved 40% monomer conversion after 2 h of irradiation. Methylene blue achieved only 31% monomer conversion, whereas **BEY** reached 83% monomer conversion within the same irradiation time (Fig. S22).

Based on these findings, we propose a reductive quenching mechanism involving photoexcitation, ISC, SET, and subsequent regeneration of **BEY** (Fig. 7, highlighted in blue). In this process, ^{3}**BEY*** accepts a single electron from TEOA through a SET process, producing **BEY** radical anion and the TEOA radical cation species. The TEOA radical cation subsequently undergoes deprotonation to form a neutral TEOA radical ($TEOA^{\cdot}$) species, which initiates polymerization. Meanwhile, the **BEY** radical anion is protonated to yield BEYH radical species ($BEYH^{\cdot}$), which is then regenerated to **BEY** through a reverse hydrogen atom transfer (RHAT) process with $TEOA^{\cdot}$ under an argon atmosphere.[55–57] In the presence of O_2, photocatalytic activity is enhanced through accelerated regeneration of **BEY**. Specifically, the **BEY** radical anion and $BEYH^{\cdot}$ species are oxidized back to **BEY** *via* a SET process with O_2 and a RHAT process with peroxy-radicals generated from oxygen-inhibition reactions, respectively.[58] In addition, the TEOA radical cation can react with oxygen to generate superoxide and iminium cations.[59]

The photopolymerization was also conducted in the presence of diphenyliodonium (IOD), which serves as a co-initiator though its role as an electron acceptor.[60,61] IOD exhibited slightly lower reactivity than TEOA for BFLs (Table 2, entries 11–14). For example, at 0.1 mM **BEY**, the monomer conversion reached 69% after 5 h of the irradiation and 90% after 9 h, yielding PEGMA with M_n of 204 kDa ($Đ = 10$) (Fig. S23). At 0.2 mM **BEY**, the monomer conversion reached 91% after 5 h and 96% after 7 h, resulting in PEGMA with M_n of 175 kDa ($Đ = 8.5$). Overall, while IOD afforded PEGMA with higher M_n values than TEOA, achieving a comparable reaction rate required a higher concentration of **BEY**. These results indicate that the initiation efficacy of IOD is lower than that of TEOA with in this photoredox system.

To verify this, we determined the initiation efficiency (Φ_i), defined as the initiation rate per the light absorption ($\Phi_i = R_i/I_a$). The initiation rate (R_i) was obtained using the inhibition period method.[62] In brief, the concentration of 2,2,6,6-tetramethylpiperidine-1-oxyl (TEMPO), employed as a radical inhibitor, was plotted against the inhibition time (t_{inh}) (Fig. 8a). As the inhibitor concentration increased, the inhibition time increased proportionally (Fig. S24). The R_i value was then calculated from the inverse slope of this plot (*i.e.*, [TEMPO])/t_{inh}). For example, in the presence of TEOA (100 mM) and OEGMA (250 mM), the R_i values were 1.7 (±0.2) × 10^{-7} M s^{-1} for **BEY** (0.01 mM) and 1.7 (±0.3) × 10^{-6} M s^{-1} for **BEY** (0.1 mM) (Fig. 8c). These results indicate that increasing the **BEY** concentration shorten the inhibition time and consequently increased the R_i value. However, IOD exhibited a much lower R_i of 4.2 (±0.3) × 10^{-8} M s^{-1}, even at 0.2 mM **BEY** under the same reaction conditions. As negative controls, no monomer conversion was observed under the optimized reaction conditions in the dark after 24 h. Similarly, no conversion was

 © 2026 The Author(s). Published by the Royal Society of Chemistry

Open Access Article. Published on 09 March 2026. Downloaded on 3/10/2026 10:21:03 PM.
This article is licensed under a Creative Commons Attribution-NonCommercial 3.0 Unported Licence.

Table 2 Free-radical photopolymerization of OEGMA with different BFLs under red or near-infrared (NIR) LED light irradiation and diverse reaction conditions[a]

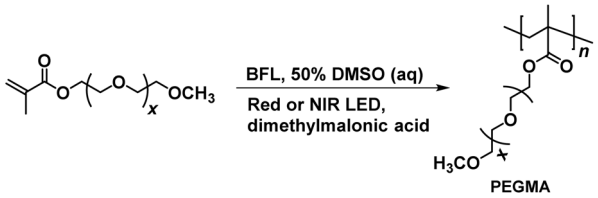

Entry	Type of BFL	[OEGMA] : [co-initiator] : [BFL] (mM)	Type of co-initiator	Conv.[b] (%)	Irradiation time (h)	$M_{n,\mathrm{exp}}$[c] (kDa)	$Đ$[c]	LED source	Atm.
1	**CB**	250 : 100 : 0.01	TEOA	6	5	56	3.2	Red	Air
2	**BBF**	250 : 100 : 0.01	TEOA	77	5	108	3.4	Red	Air
3	**BEY**	250 : 100 : 0.01	TEOA	84	5	114	3.4	Red	Air
4	**BBF**	250 : 100 : 0.1	TEOA	91	5	60	2.7	Red	Air
5	**BEY**	250 : 100 : 0.1	TEOA	96	5	24	2.6	Red	Air
6	none	250 : 100 : 0	TEOA	0	24	<1	n.a.	Red	Air
7	**BEY**	250 : 100 : 0.1	TEOA	0	24	<1	n.a.	none	Air
8	**BEY**	250 : 100 : 0.1	TEOA	73	5	19	2.5	Red	Ar[f]
9	**BEY**	250 : 100 : 0.1	TEOA	92	5	21	2.4	Red	O_2[f]
10	**BEY**	250 : 100 : 0.1	TEOA	93	7	22	2.6	NIR[e]	Air
11	**CB**	250 : 100 : 0.2	IOD	0	7	<1	n.a.	Red	Air
12	**BBF**	250 : 100 : 0.2	IOD	90	7	174	8.6	Red	Air
13	**BEY**	250 : 100 : 0.2	IOD	96	7	175	8.5	Red	Air
14	**BEY**	250 : 100 : 0.1	IOD	90	9	204	10	Red	Air
15	none	250 : 100 : 0	IOD	0	24	<1	n.a.	Red	Air
16	**BEY**	250 : 100 : 0.2	IOD	0	24	<1	n.a.	none	Air
17	**BEY**	250 : 100 : 0.2	IOD	70	7	≥767[d]	>4	Red	Ar[f]
18	**BEY**	250 : 100 : 0.2	IOD	92	7	153	>10	Red	O_2[f]

[a] Photopolymerization was typically conducted in a standard NMR tube sealed with a cap, containing 0.6 mL of a 1 : 1 (v/v) mixture of DMSO and D_2O under aerobic conditions at room temperature. [b] Monomer conversion (%) was determined by ^{1}H NMR using dimethylmalonic acid as an internal standard, as detailed in the SI. [c] Experimental molecular weights and polydispersity ($Đ$) were determined by GPC analysis using PMMA standards for calibration with DMF containing 1 mM LiBr as the eluent as detailed in the SI. [d] The upper detection limit. [e] NIR LED (730 ± 30 nm, 12.5 W cm^{-2}). [f] A J-Young NMR tube equipped with a valve was used for reactions under Ar (g) and O_2 (g) atmospheres. IOD: diphenyliodonium, n.a.: not applicable.

observed in the absence of BFLs after 24 h of irradiation (Table 2, entries 15 and 16) (Fig. S25).

The light absorption (I_a) was calculated using the Beer–Lambert law [$I_a = I_0\ (1-10^{-\varepsilon bc})$], where I_0 is the incident light determined by chemical actinometry, ε is the molar absorptivity of **BEY**, b is the cuvette path length (1.0 cm), and c is the corresponding molar concentration of **BEY** (detailed in the SI and Fig. S26a).[63] The calculated I_a values were 6.6 (±0.6) × 10^{-7} M s^{-1} for **BEY** (0.01 mM), 4.4 (±0.4) × 10^{-6} M s^{-1} for **BEY** (0.1 mM), and 5.9 (±0.5) × 10^{-6} M s^{-1} for **BEY** (0.2 mM). Accordingly, the Φ_i values were 0.3 (±0.1) for **BEY** (0.01 mM), 0.4 (±0.2) for **BEY** (0.1 mM) in the presence of TEOA (100 mM) (Fig. 8c). In contrast, when IOD exhibited a significantly lower Φ_i (<0.01) was observed, even at an elevated **BEY** concentration (0.2 mM). Consequently, these results demonstrate that the diminished polymerization rate in the presence of IOD arises from its low initiation efficiency, presumably due to less favorable photoinduced electron transfer interaction with BFLs.

The photopolymerization of OEGMA with **BEY** in the presence of IOD was also carried out under different atmospheric conditions (Table 2, entries 17 and 18). Compared to ambient atmosphere, monomer conversion decreased considerably under an argon atmosphere. For example, at **BEY** (0.2 mM), monomer conversion reached 70% ($k_{\mathrm{app}} = 0.6 \times 10^{-4}$ s^{-1}) after 7 h of irradiation, which interestingly resulted in partial hydrogel formation. This result was reproducible across multiple trials. Under an oxygen-rich atmosphere, however, monomer conversion recovered to 92% ($k_{\mathrm{app}} = 1.1 \times 10^{-4}$ s^{-1}), yielding PEGMA with M_n = 153 kDa ($Đ$ > 10) (Fig. S27). These observations further conform that O_2 accelerates this photopolymerization. Based on these findings, we propose an oxidative quenching mechanism (Fig. 7, highlighted in red). Under an argon atmosphere, ^{3}**BEY***donates a single electron to IOD through a SET process, generating the **BEY** radical cation (**BEY**$^{\cdot+}$) and the IOD radical species ($Ar_2I^{\cdot}$). This process is supported by negative ΔG_{PET} values (−0.75 to −0.78 eV). The IOD radical undergoes bond cleavage to produce a phenyl radical ($Ar^{\cdot}$), which initiates polymerization. The resulting **BEY** radical cation is reduced to the BEYH through a HAT process from the propagating polymer radical ($P_n^{\cdot}$), forming a polymerizable macromonomer. This macromonomer further participates in free-radical polymerization, leading to hydrogel

Open Access Article. Published on 09 March 2026. Downloaded on 3/10/2026 10:21:03 PM.
This article is licensed under a Creative Commons Attribution-NonCommercial 3.0 Unported Licence.

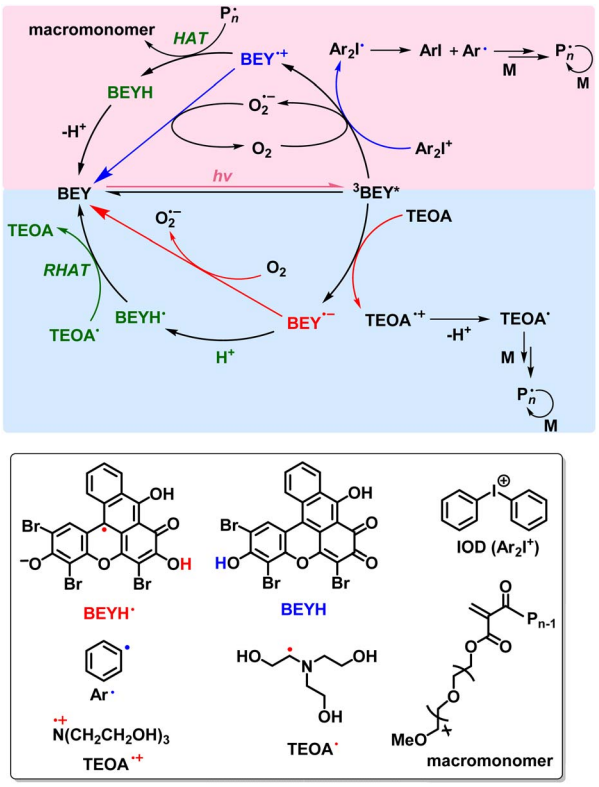

Fig. 7 Plausible mechanism of photoinitiated free-radical polymerization involving oxidative (top) and reductive (bottom) quenching cycles in the presence and absence of O_2. HAT: hydrogen atom transfer, RHAT: reverse hydrogen atom transfer.

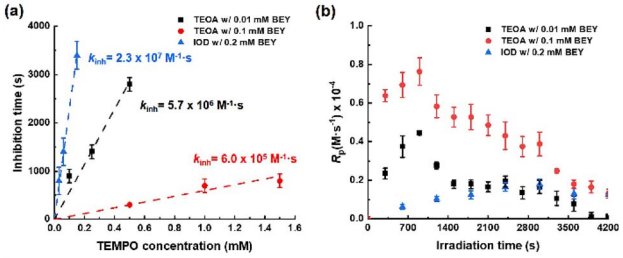

(c)

Conc. of BEY (mM)	Type of co-initiator	R_i (M·s^{-1}) x 10^{-7}	I_a(M·s^{-1}) x 10^{-7}	Φ_i (R_i/I_a)	R_p (M·s^{-1}) x 10^{-5}	Kinetic chain length	Φ_{rxn}
0.01	TEOA	1.7±0.2	6.6±0.6	0.3±0.1	4.4±0.7	259±51	-
0.1	TEOA	17±3	43±4	0.4±0.2	7.2±0.6	42±8	17.4±0.7
0.2	IOD	0.4±0.03	59±5	< 0.01	1.7±0.6	405±146	2.4±0.1

Fig. 8 Comparison of kinetic parameters at different BEY concentrations and co-initiators under ambient conditions: (a) plots of inhibition time *versus* TEMPO concentration, (b) correlation of propagation rate (R_p) with irradiation time, and (c) summary of the experimentally determined values. TEMPO: 2,2,6,6-tetramethylpiperidine-1-oxyl, R_i: initiation rate, I_a: light absorption, Φ_i: initiation efficiency, and Φ_{rxn}: reaction quantum yield.

formation. The BEYH is regenerated to **BEY** through proton transfer, completing the catalytic cycle. In the presence of O_2, ^{3}**BEY***also donates a single electron to O_2, generating superoxide ($O^{\cdot-}$) and the **BEY** radical cation. The superoxide then reduces the **BEY** radical cation *via* a SET process, thereby accelerating the regeneration of **BEY**. In contrast, excessive amounts of O_2 reduce the polymerization rate relative to that observed under ambient conditions, presumably by suppressing the SET pathway between ^{3}**BEY*** and IOD.

The reliability of the measured molecular weights can be evaluated by comparison with the theoretical degree of polymerization (DP). The theoretical DP can be estimated from the kinetic chain length, defined as the ratio of the propagation rate (R_p) to the initiation rate (R_i).[64] Specifically, the maximum R_p ($R_{p,max}$) was used to determine the kinetic chain length.[65] The kinetic chain length was examined under varying **BEY** concentrations and different initiator types. The $R_{p,max}$ values, determined by ^{1}H NMR spectroscopy, were found to depend on both the concentration of **BEY** and the type of initiator (Fig. 8b). As the **BEY** concentration increased, $R_{p,max}$ value also increased. For example, in the presence of TEOA, increasing **BEY** from 0.01 mM to 0.1 mM increased $R_{p,max}$ from 4.4 (±0.7) × 10^{-5} M s^{-1} to 7.2 (±0.6) × 10^{-5} M s^{-1} (Table 2, entries 3 and 5). However, IOD exhibited a lower $R_{p,max}$ of 1.7 (±0.6) × 10^{-5} M s^{-1} at 0.2 mM **BEY** (Table 2, entry 13) (Fig. 8c). Accordingly, the kinetic chain lengths, calculated from $R_{p,max}$ values and the corresponding R_i values, were 259 (±51) for entry 3, 42 (±8) for entry 5, and 405 (±146) for entry 13 in Table 2. These kinetic chain lengths are in good agreement with the experimentally determined $M_{n,GPC}$ values, indicating that disproportionation is the predominant termination pathway in this chain radical polymerization.

We also determined reaction quantum yields to elucidate mechanistic features of these photoredox processes involving radical-chain propagation. The reaction quantum yield (Φ_{rxn}) is defined as the number of products formed ($N_{products}$) per the number of photons absorbed at a specific wavelength ($N_{photons}$).[66] In photoinitiated free-radical polymerization, which proceeds thorough a chain-propagating mechanism, each absorbed photon can initiate multiple product-forming events; thus, Φ_{rxn} is expected to exceed 1.[67] The number of photons absorbed by the sample was determined by chemical actinometry using Reinecke's salt as a reference for 660 nm (detailed in the SI).[68] The number of products formed was quantified by ^{1}H NMR spectroscopy. The Φ_{rxn} values depended on both the type of BFL and the co-initiator. For example, reaction quantum yields were 17.4 (±0.7) for **BEY**, 7.1 (±0.5) for **BBF**, and 1.8 (±0.2) for **CB** under the same reaction conditions (0.1 mM BFL + 100 mM TEOA + 250 mM OEGMA) (Fig. 8c, S26b and c). In comparison, when IOD was used as the co-initiator, a lower quantum yield (Φ_{rxn} = 2.4 ± 0.1) was observed, even at a higher **BEY** concentration (0.2 mM). These results are consistent with the observed trends in photocatalytic performance.

To expand the monomer scope, we investigated the polymerization of several water-soluble monomers using **BEY** in the presence of TEOA under the optimized conditions as described in Table 3. Under an ambient atmosphere, 3-sulfopropy methacrylate (SPMA) and AMPS achieved monomer conversions of 93% (k_{app} = 1.8 × 10^{-4} s^{-1}) with M_n of 5 kDa ($Đ$ > 10) and 82% (k_{app} = 1.0 × 10^{-4} s^{-1}) with M_n of 7 kDa ($Đ$ > 10), respectively. The polymerization of 2-hydroxyethyl methacrylate (HEMA) and

 © 2026 The Author(s). Published by the Royal Society of Chemistry

Open Access Article. Published on 09 March 2026. Downloaded on 3/10/2026 10:21:03 PM.
This article is licensed under a Creative Commons Attribution-NonCommercial 3.0 Unported Licence.

Table 3 Investigation of monomer scope in the BEY/TEOA system under aerobic conditions with red LED light irradiation[a]

Entry	Monomer	Conv.[b] (%)	Irradiation time (h)	$M_{n,\mathrm{exp}}$[c] (kDa)	$Đ$[c]
1	SPMA	93	7	5	>10
2	AMPS	82	8	7	>10
3	HEMA	81	4 (sat.)	3	6
4	NIPAm	61	4 (sat.)	6	8

[a] Photopolymerization was conducted in a standard NMR tube sealed with a cap under aerobic conditions at room temperature. The reaction solution consisted of **BEY** (0.1 mM), TEOA (100 mM), and monomer (250 mM) dissolved in 50% DMSO (aq) (total volume: 0.6 mL). [b] Monomer conversion (%) was determined by ^{1}H NMR using dimethylmalonic acid as an internal standard. [c] Experimental molecular weights and polydispersity ($Đ$) were determined by GPC analysis using PMMA standards for calibration with DMF containing 1 mM LiBr as the eluent. SPMA: 3-sulfopropy methacrylate, AMPS: 2-acrylamido-2-methyl-1-propanesulfonate, HEMA: 2-hydroxyethyl methacrylate, NIPAm: *N*-isopropylacrylamide, and sat.: saturation.

N-isopropylacrylamide (NIPAm) reached a plateau after 4 h of irradiation, resulting in monomer conversions of 81% ($k_{\mathrm{app}} = 1.7 \times 10^{-4}\ \mathrm{s}^{-1}$) with M_n of 3 kDa ($Đ = 6$) and 61% ($k_{\mathrm{app}} = 1.1 \times 10^{-4}\ \mathrm{s}^{-1}$) with M_n of 6 kDa ($Đ = 8$), respectively (Fig. S28). These results indicate that, despite high monomer conversion, the molecular weights were relatively lower than expected, presumably due to limited solubility of the resulting polymers in the solvent system.[69]

Analysis using time-resolved photoluminescence and electrochemical potentials

To support the proposed mechanism, we characterized the photophysical and electrochemical properties of the BFLs (Table 4). In particular, these experimental values were primarily used to calculate the Gibbs free energy of photoinduced electron transfer (ΔG_{PET}), which represents the driving force for intermolecular electron transfer between BFLs and the co-initiators, as described by Marcus theory.[70] The ΔG_{PET} can be expressed as:

$\Delta G_{\mathrm{PET}} = -F(\Delta E) = -F\,(E_{\mathrm{red}} - E_{\mathrm{ox}}) = -F\,[E_{\mathrm{red}}(\mathrm{A}/\mathrm{A}^{\cdot-}) - E_{\mathrm{ox}}(\mathrm{D}^{\cdot+}/\mathrm{D})] - w - E^{\mathrm{S/T}}{}_{0,0}$, where F is the Faraday constant, w is the electrostatic work term (often neglected), $E^{\mathrm{S/T}}{}_{0,0}$ is typically estimated from the wavelength of maximum phosphorescence (λ_{p}), and A and D denote the acceptor and donor, respectively. Because BFLs donate a single electron to either CTA or IOD from their triplet-excited state, ΔG_{PET} can be calculated using the following equation: $\Delta G_{\mathrm{PET}} = -F[E_{\mathrm{red}}(A/A^{\cdot-}) - E^{*}_{\mathrm{ox}}(\mathrm{BFL}^{\cdot+}/\mathrm{BFL})]$, where $E^{*}_{\mathrm{ox}}(\mathrm{BFL}^{\cdot+}/\mathrm{BFL}) = E_{\mathrm{ox}}(\mathrm{BFL}^{\cdot+}/\mathrm{BFL}) - E^{\mathrm{T1}}_{0,0}$, where E and E^{*} are ground- and excited-state energies, respectively. Initially, we determined the oxidation potential of the BFLs and the reduction potential of the acceptors by linear sweep voltammetry (detailed in the SI). In particular, the oxidation potentials of the BFLs showed a slight deceasing trend: **CB** (0.11 eV), **BBF** (0.09 eV), and **BEY** (0.08 eV) (Fig. S29). The reduction potentials of CTA (**1**) and IOD were measured to be −1.08 eV and −0.73 eV, respectively (Fig. S30). Furthermore, phosphorescence spectra were obtained by time-resolved photoluminescence measurements (FLS1000, Edinburgh Instruments Ltd, UK) at 77 K (detailed in the SI). The λ_{p} values were 765 nm for **CB**, 788 nm for **BBF**, and 795 nm for **BEY** (Fig. 9a). The corresponding lifetimes were measured as major components of 0.4 (±0.1) ms (78% of the decay) for **BEY** and 3.7 (±0.8) ms (83% of the decay) for **BBF**, while that of **CB** was negligible (Fig. 9b and S31). These relatively long lifetimes confirm that the emissions of both **BBF** and **BEY** originate from phosphorescence.

Accordingly, the calculated ΔG_{PET} values between BFLs and CTA ($\Delta G_{\mathrm{PET,CTA}}$) were −0.43 eV for **CB**, −0.40 eV for **BBF**, and −0.40 eV for **BEY**. Additionally, the calculated ΔG_{PET} values for BFLs and IOD ($\Delta G_{\mathrm{PET,IOD}}$) were −0.78 eV for **CB**, −0.75 eV for **BBF**, and −0.75 eV for **BEY**. These negative values indicate that PET processes of the BFLs with either CTA (**1**) or IOD is

Table 4 Summary of photophysical and electrochemical properties of BFLs[a]

	CB	BBF	BEY
$\lambda_{\mathrm{ex,vis}}$(nm)[a]	600	605	620
ε (cm^{-1} M^{-1})[b]	1225	1385	1340
$\lambda_{\mathrm{F,vis}}$(nm)[a]	740	770	740
Φ_{f} [a,c]	< 0.01	< 0.01	< 0.01
τ_{F}(ns)[a]	2.1(±0.1,26%) 6.7(±0.3,74%)	3.1(±0.1,6%) 7.2(±1.2,94%)	2.3(±0.3,12%) 8.3(±0.1,88%)
λ_{p}(nm)[a,d]	765	788	795
τ_{P}(ms)[a,d]	n.a.	0.6 (±0.2,17%) 3.7 (±0.8,83%)	0.1 (±0.1,22%) 0.4 (±0.1,78%)
$E^{\mathrm{T1}}{}_{0,0}$ (eV)	1.62	1.57	1.56
$E^{\mathrm{ox}}{}_{1/2}$ (V/SCE)[e]	0.11	0.09	0.08
$\Delta G_{\mathrm{PET,CTA}}$ (eV)	−0.43	−0.40	−0.40
$\Delta G_{\mathrm{PET,IOD}}$ (eV)	−0.78	−0.75	−0.75
$E^{\mathrm{red}}{}_{1/2}$ (V/SCE)[e]	−0.36	−0.35	−0.36
$\Delta G_{\mathrm{PET,TEOA}}$ (eV)	−0.31	−0.27	−0.25
pK_{a0} [f]	1.69	n.a.	n.a.
pK_{a1} [f]	6.03	4.22 (6.54)[g]	3.19
pK_{a2} [f]	n.a.	n.a.	5.8

[a] 0.1 mM BFL in a mixture of ethanol and DMSO (90 : 10, v/v) containing 10 mM NaOH. [b] 100 μM BFL in 50% DMSO (aq) containing pH 11 buffer solution. [c] Absolute quantum yield (detailed in the SI). [d] Measured under cryogenic conditions. [e] 1 mM BFL in 50% DMSO (aq) containing 10 μM NaOH. [f] Measured in a mixed solvent (DMSO : pH buffer (aq) = 10 : 90, v/v). [g] Bridged monobromofluorescein, n.a.: not applicable.

Open Access Article. Published on 09 March 2026. Downloaded on 3/10/2026 10:21:03 PM.
This article is licensed under a Creative Commons Attribution-NonCommercial 3.0 Unported Licence.

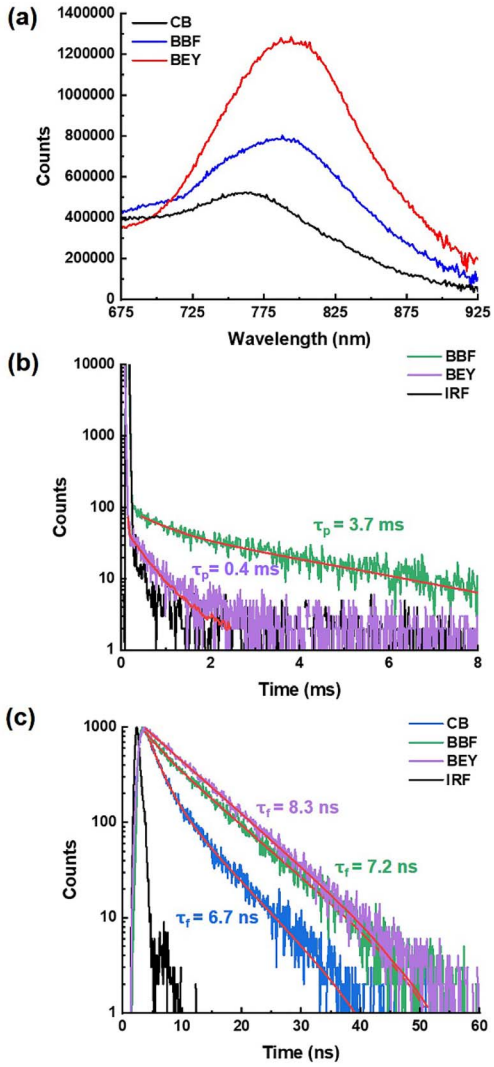

Fig. 9 Photoluminescence spectra of BFLs in ethanol: (a) time-gated phosphorescence spectra of BFLs at 77 K with a delay time of 2 ms, (b) phosphorescence decay profiles of **BBF** and BEY at 77 K, where **CB** showed negligible emission counts. Red lines represent the best–fit curves, and the black line denotes the instrument response function (IRF), and (c) fluorescence decay profiles of BFLs at 77 K, with red lines representing the best–fit curves and the black line indicating IRF.

thermodynamically favorable. Furthermore, the small differences of these values within each system suggest that the corresponding PET rate constants for **CB**, **BBF**, and **BEY** are comparable. On the other hand, ΔG_{PET} of BFLs with TEOA can be determined the following equation: $\Delta G_{PET} = -F[E^*_{red}(BFL/BFL^{\cdot-}) = E_{ox}(TEOA/TEOA^{\cdot+})]$, where $E^*_{red}(BFL/BFL^{\cdot-}) = E_{red}(BFL/BFL^{\cdot-}) + E^{T1}_{0,0}$ The oxidation potential of TEOA was measured to be 0.95 eV (Fig. S32). The reduction potentials of BFLs were similar, with values of −0.36 eV for **CB**, −0.35 eV for **BBF**, and −0.36 eV for **BEY** (Fig. S33). Therefore, the calculated ΔG_{PET} values for BFLs and TEOA ($\Delta G_{PET,TEOA}$) were −0.31 eV for **CB**, −0.27 eV for **BBF**, and −0.25 eV for **BEY**.

The ΔG_{PET} values for **CB**, **BBF**, and **BEY** were indistinguishable within each electron-transfer system, indicating that these parameters alone are insufficient to explain the pronounced differences in their photocatalytic activity. In contrast, the phosphorescence intensities of the BFLs showed significant variation. Under identical measurement conditions, the emission intensity followed the trend **CB** < **BBF** < **BEY**. For example, **BEY** exhibited approximately twice the intensity of **BBF** and three times that of **CB**, presumably due to the heavy-atom effect. As a heavy halogen atom, bromine enhances the spin-orbital coupling (SOC) effect, thereby facilitating ISC and resulting in stronger phosphorescence.[71,72] We previously demonstrated that incorporation of bromine atoms into fluorescein increases its photocatalytic performance.[38] Therefore, the phosphorescence intensity reflects the population of the triplet-excited state, which contributes to the superior photoredox catalytic performance of **BEY**. In addition to phosphorescence, fluorescence lifetimes at 77 K were measured to be values of 6.7 (±0.3) ns (74% of the decay) for **CB**, 7.2 (±1.2) ns (94% of the decay) for **BBF**, and 8.3 (±0.1) ns (88% of the decay) for **BEY** (Fig. 9c and S34). Taken together, **BEY** exhibits superior properties, including stronger absorptivity in the red-light range and higher phosphorescence intensity, which collectively contribute to its improved photoredox catalytic performance.

The protolytic equilibria of BFLs were studied in an aqueous solution (DMSO : pH buffer solution = 10 : 90, v/v) to determine their dissociation constants (pK_a), which describe the relative concentration of each protolytic species as a function of pH. For example, **CB** displays three different ionization states such as cationic, neutral, and monoanionic state corresponding to pK_{a0} and pK_{a1}, whereas **BEY** exhibits neutral, monoanionic, and dianionic states corresponding to pK_{a1} and pK_{a2} within the pH range of 1.0–10.0. The protolytic equilibria and pK_a values of the BFLs were simulated using DATAN software (Fig. S35–S37). Based on the simulation results, BFLs predominately exist in their anionic forms at pH values above 8.0. Notably, the presence of bromine substituent(s) lowers pK_a values of the BFLs, making pK_{a0} difficult to observe within the measurable range. In the case of **BBF**, two pK_{a1} values were assigned to bridged dibromo- and monobromo-fluorescein, as inferred from changes in the UV-vis absorption spectra under varying pH conditions.

Analysis of electron paramagnetic resonance (EPR) spectroscopy

It has been known that various radical species are generated during the photochemical reactions of fluorescein derivatives.[32,73,74] Direct observation of such radical species is challenging at room temperature due to their inherent instability. In this study, we performed spin-trap EPR spectroscopy to track radical species generated during the photochemical reaction of **BEY** under red-light irradiation. 5,5-Dimethyl-1-pyrroline-*N*-oxide (DMPO) was used as a spin-trapping agent because it forms relatively stable spin-adducts producing radical-specific EPR features.[75,76]

Fig. 10 displays the EPR spectra obtained from the mixture solutions containing **BEY** (1 mM) + DMPO (0.1 M) + each co-initiator (0.1 M TEOA, IOD, or CTA (**1**)) after 20 min of red-

 © 2026 The Author(s). Published by the Royal Society of Chemistry

Open Access Article. Published on 09 March 2026. Downloaded on 3/10/2026 10:21:03 PM.
This article is licensed under a Creative Commons Attribution-NonCommercial 3.0 Unported Licence.

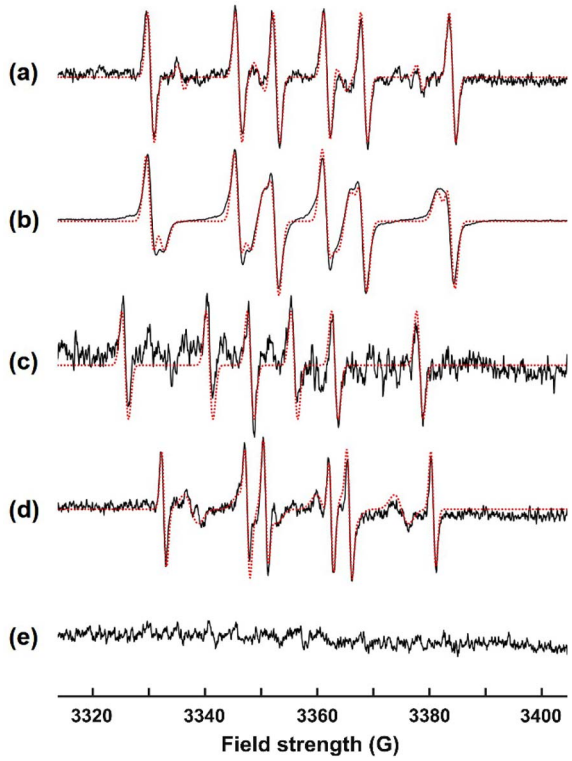

Fig. 10 EPR spectra (black lines) obtained from the solutions of (a) **BEY** + DMPO, (b) **BEY** + DMPO + TEOA, (c) **BEY** + DMPO + IOD, (d) **BEY** + DMPO + CTA (**1**), and (e) DMPO after 20 min of red-light irradiation in 50% DMSO (aq). The corresponding simulations (red dots) are overlaid on the experimental spectra. Detailed simulations are represented in Fig. S38.

light irradiation in 50% DMSO (aq). All of the solutions containing **BEY** gave rise to EPR signals, indicating that **BEY** is responsible for the generation of radicals. The EPR spectra were well fitted by numerical simulations (Fig. 10), and their simulated EPR parameters are summarized in Table 5. The observed isotropic nuclear hyperfine coupling constants (A) could be grouped into two: one with $A_N < A_H$, and the other with $A_N > A_H$. Here, A_N and A_H denote A of nitrogen nucleus and proton, respectively. Previous EPR studies on DMPO-spin adducts have found that $A_N < A_H$ cases were arising from carbon-centered radicals (C*) while $A_N \geq A_H$ was characteristic of oxygen-centered radicals (O*).

The EPR spectrum of the mixture solution of **BEY** + DMPO exhibits two radical EPR signals (Fig. 10a). The characteristics of A_N (15.7 G) < A_H (22.4 G) of the major signal suggest that the radical is C-centered. And the A_N and A_H values are close to the reported ones for the DMPO-C* adducts.[32] We assume that the photochemical reaction of **BEY** with O_2 leads to the formation of hydroxyl radical ($^{\cdot}$OH). This reactive species decomposes DMSO to form methyl radical ($^{\cdot}$CH3), yielding the DMPO-CH_3 adduct.[46] The DMPO-OH was observed as a minor signal in the spectrum. Interestingly, DMPO-OH signal is very weak, which is consistent with our previous finding that this adduct is susceptible to decomposition or rearrangement under photoredox catalysis.[32]

Two EPR signals are also identified in the spin-trap EPR of **BEY** + DMPO + TEOA (Fig. 10b). The major signal is identical to the EPR parameters of DMPO-CH_3 observed in **BEY** + DMPO. A_N (15.5 G) and A_H (19.6 G) values derived from the minor EPR signal are very close to our previously reported hyperfine constants of the DMPO-C* generated in fluorescein derivative + DMPO + TEOA mixture,[32,73] suggesting that the detected C-centered radical is derived from TEOA ($^{\cdot}$TEOA). The EPR spectrum of **BEY** + DMPO + IOD mixture shows a signal with A values close to DMPO-CH_3 of **BEY** + DMPO and **BEY** + DMPO + TEOA (Fig. 10c). Though the observed A values are close to those of DMPO-CH_3, the spectral feature is clearly distinguished from the spectra of DMPO-CH_3 and the hyperfine coupling constants closely matches the reported parameters for the DMPO-Ph adduct,[77] supporting that **BEY** + DMPO + IOD generated DMPO-Ph.

The EPR spectrum (Fig. 10d) obtained from **BEY** + DMPO + CTA (**1**) are also resolved into two radical EPR signals: one with A_N (14.9 G) < A_H (18.2 G) for major intensity and the other with A_N (13.9 G) > A_H (9.6 G) for minor intensity, being consistent with that the major and minor intensities are attributed to DMPO-C* and DMPO-O*, respectively. We assume that the photochemical reaction of **BEY** with CTA (**1**) induces the cleavage of the CTA to generate 4-cyanopentanoic acid radical ($^{\cdot}$CP) species, responsible for the DMPO-C* signal.[78] A_N and A_H of the DMPO-O* signals are similar to those observed for O-centered radical species trapped by DMPO, such as DMPO-OR ($R = t$-butyl).[79] It has been reported that the carbon-based $^{\cdot}$CP radical reacted with O_2 to form an O-centered radical, such as oxy radical ($^{\cdot}$OCP).[78] Therefore, we assume that the observed DMPO-O* signal corresponds to the DMPO-OCP adduct. In summary, the spin-trap EPR investigations identified three distinct C-centered radical species, $^{\cdot}$TEOA, $^{\cdot}$Ph, and $^{\cdot}$CP, produced from the photoreaction of BEY with TEOA, IOD, and CTA (**1**), respectively. Additionally, the observation of the O-

Table 5 EPR parameters derived from the spin-trap EPR measurements

	Major			Minor			Spin adducts	
Samples	g	A_N (G)	A_H (G)	g	A_N (G)	A_H (G)	g	A_N (G)
BEY + DMPO	2.0063	15.7	22.4	2.0065	14.5	13.5	DMPO-CH_3	DMPO-OH
BEY + DMPO + TEOA	2.0064	15.7	22.4	2.0063	15.5	19.6	DMPO-CH_3	DMPO-TEOA
BEY +DMPO + IOD	2.0061	15.1	22.4	—	—	—	DMPO-Ph	—
BEY + DMPO + CTA (**1**)	2.0066	14.9	18.2	2.0068	13.9	9.6	DMPO-CP	DMPO-OCP
DMPO	No signal							

Open Access Article. Published on 09 March 2026. Downloaded on 3/10/2026 10:21:03 PM. This article is licensed under a Creative Commons Attribution-NonCommercial 3.0 Unported Licence.

centered radical species, ˙OCP, from the photoreaction of **BEY** with CTA (**1**) further supports the photo-RAFT process.

Photobleaching under various conditions

We investigated the photobleaching behavior of **BEY** under various co-initiators and atmospheric conditions, as the extent of photobleaching can provide supporting evidence for the proposed mechanism. Photobleaching was quantified by monitoring changes in the integrated absorbance of **BEY** (0.1 mM) within the 630–690 nm range, corresponding to the red LED light source, as a function of irradiation time. In the presence of CTA (**1**), no photobleaching of **BEY** was observed in the absence of irradiation (Fig. 11a). Under irradiation, the photobleaching rate under different atmospheric conditions (Table 2, entries 3, 17, and 18) followed the order: argon < ambient < oxygen-rich. For example, after 3 h of irradiation, photobleaching reached 9% under argon, 35% under an ambient atmosphere, and 44% under an oxygen-rich atmosphere.

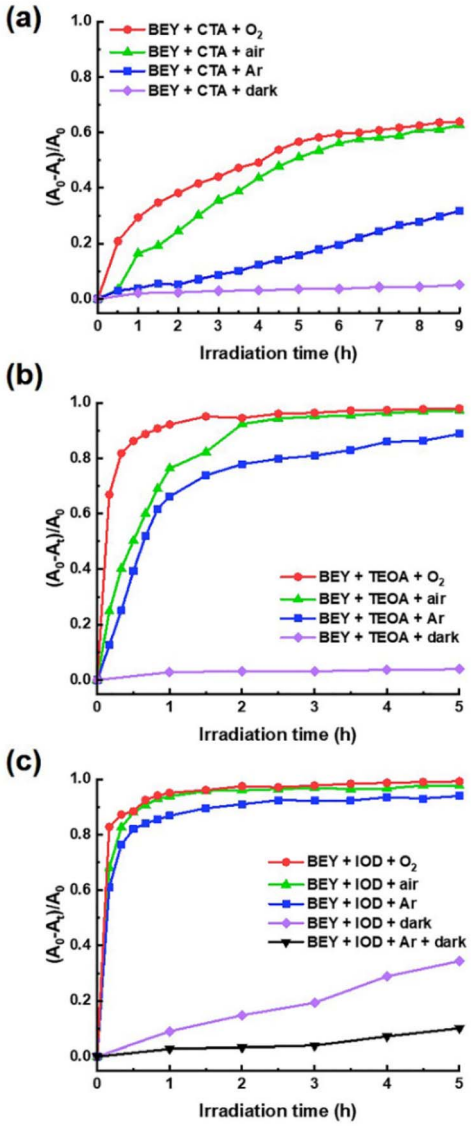

Fig. 11 Photobleaching of BFLs (0.1 mM) under different atmospheric conditions in the presence of (a) CTA (**1**, 1.25 mM), (b) TEOA (100 mM), and (c) IOD (100 mM) dissolved in 50% DMSO (aq).

A similar trend was observed for TEOA and IOD. For instance, after 1 h of irradiation with TEOA, photobleaching reached 66% under argon conditions, 76% under ambient conditions, and 92% under oxygen-rich conditions (Fig. 11b). IOD exhibited faster photobleaching of **BEY** than TEOA, presumably because it can promote **BEY** degradation even in the dark. For example, after 4 h in the dark, **BEY** bleaching reached 29% under ambient conditions and 7% under an argon atmosphere (Fig. 11c). Because no monomer conversion was observed under the optimized reaction conditions using IOD for 24 h in the dark (Table 2, entry 16), this bleaching is not associated with radical polymerization. Overall, these results align with the trends observed in monomer conversion under different atmospheric conditions and polymerization manners, suggesting that photobleaching rate correlates with polymerization rate. In general, higher photopolymerization rates are accompanied by faster photobleaching rate; however, excessively rapid (photo)bleaching can ultimately reduce polymerization rate.

In addition, quenching rate constants were determined by Stern–Volmer analysis. Because TEOA exhibited superior photocatalytic performance compared with the other co-initiators, we investigated the quenching behavior between the BFLs and TEOA in 50% DMSO (aq) under ambient conditions using fluorometry (detailed in the SI). As a result, the quenching rate constants (k_q) were 5.2 (±0.5) × 10^8 M^{-1} s^{-1} for **BEY**, 4.9 (±0.8) × 10^8 M^{-1} s^{-1} for **BBF**, and 3.9 (±0.2) × 10^8 M^{-1} s^{-1} for **CB** (Fig. S39).

Stimulus-responsive CB for polymerization-based amplification

Motivated by the robust red-light photoredox activity of BFLs, we developed a strategy for switchable photoredox catalysis using a stimulus-responsive photoredox catalyst. As a proof of concept, we designed and synthesized sulfonyl-protected **CB** (**2**) as a fluoride ion (F^-)–selective "turn-on" photoredox catalyst (Fig. 12). Fluoride ions are well known to selectively cleave sulfonyl protecting groups in solution.[80] Briefly, compound (**2**) was synthesized by nucleophilic acyl substitution reaction of **CB** with *p*-nitrobenzenesulfonyl chloride in methylene chloride, affording a reddish solid in 50% yield (detailed in the SI). In DMSO, compound (**2**) (50 μM) exhibited a distinct red color, in contrast to the green color of **CB** (50 μM).

The structure of (**2**) was confirmed by NMR and mass spectrometry, followed by analysis using UV-vis spectrometry. Compared with **CB**, (**2**) exhibited a blue-shifted absorption maximum (λ_{max} = 513 nm) and markedly weaker absorption in the red-light region. However, upon addition of fluoride ions, (**2**) showed a strong absorption band (λ_{max} = 710 nm) in the red-light region, indicating formation of **CB** through fluoride-induced cleavage of the sulfonyl ester bond. Fig. 13a exhibits the time-dependent UV-vis spectra of (**2**) (50 μM) in DMSO at room temperature after addition of tetrabutylammonium

 © 2026 The Author(s). Published by the Royal Society of Chemistry

Open Access Article. Published on 09 March 2026. Downloaded on 3/10/2026 10:21:03 PM.
This article is licensed under a Creative Commons Attribution-NonCommercial 3.0 Unported Licence.

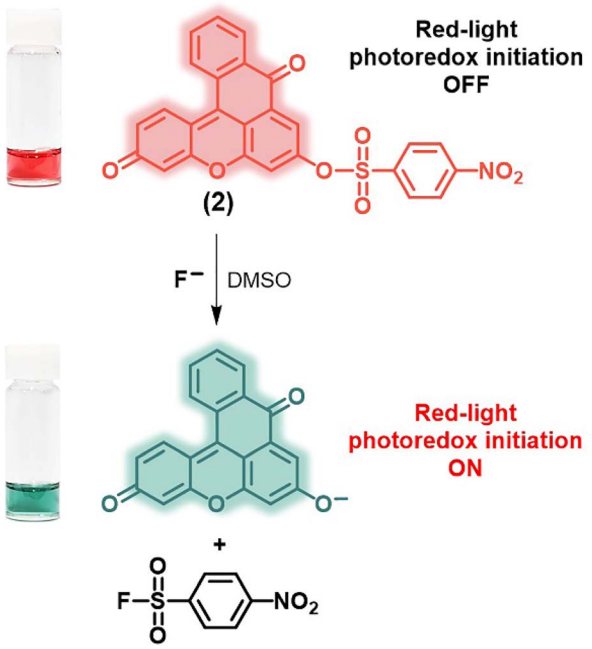

Fig. 12 Schematic depiction of the selective reaction of sulfonyl-protected CB (2) with fluoride ion. The vial images exhibit the solution before and after the addition of fluoride ion.

fluoride (TBAF) (1 equiv.) as the fluoride ion source. Over time, the characteristic absorption band at 710 nm corresponding to **CB** increased, while the band at 510 nm associated with (**2**) decreased. The reaction reached a plateau after 50 min at room temperature and 15 min at 37 °C, yielding 96% conversion (Fig. 13b). In 50% DMSO (aq), the conversion reached only 5% with10 equiv. of fluoride ions and was negligible with 1 equiv. after 1 h at room temperature under otherwise identical conditions (Fig. S40). This behavior can be attributed to the diminished nucleophilicity of fluoride ions in aqueous solution due to hydrogen-bonding interactions.[81]

The switchable red-light photoredox catalytic behavior of (**2**) was demonstrated through photoinitiated, free-radical polymerization of poly(ethylene glycol) diacrylate (PEGDA, 0.6 M) with TEOA (0.75 M) in 20% DMSO (aq). PEGDA was chosen as a crosslinking monomer because it rapidly forms hydrogels through radical polymerization, enabling catalytic efficacy to be evaluated by the naked eye.[82] As a positive control, hydrogel formation was observed within 15 min of the irradiation at 7.5 μM of **CB**. In addition, 15 μM of **CB** rapidly formed a hydrogel within 8 min, whereas no gelation was observed at 5 μM of **CB** even after 1 h of irradiation (Fig. S41). Following complete conversion of the reaction of (**2**) upon reaction with fluoride ions, the resulting solution was diluted to **CB** concentrations of 10, 7.5, and 5 μM, as determined using the Beer–Lambert law using the molar absorptivity of **CB**. Each diluted solution in a vial was then subjected to photopolymerization with PEGDA under red-light irradiation in aerobic conditions. Upon inversion of the vials, the red-stained hydrogel remained at the top, while the unreacted, residual solution settled at the bottom (Fig. 13c). For example, hydrogel formation occurred within 20

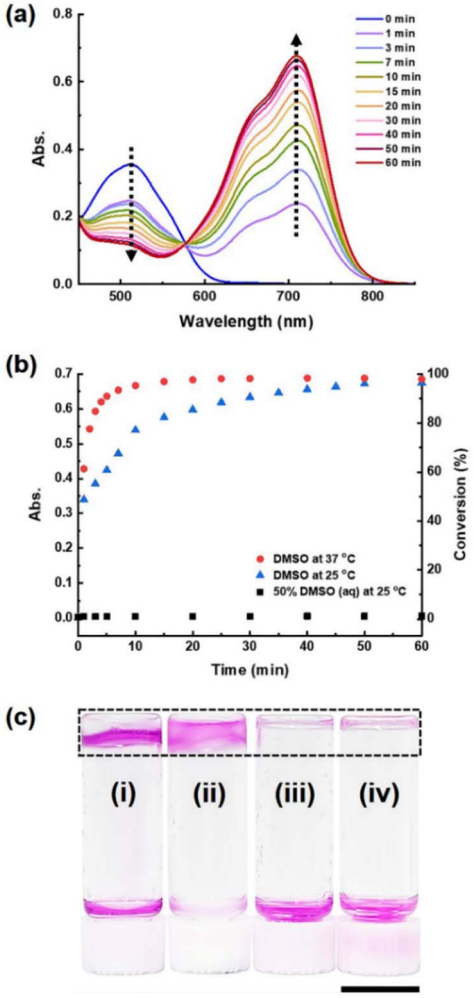

Fig. 13 (a) UV-vis absorption spectra for the kinetic study of the reaction between (**2**) (50 μM) and fluoride ions (1 equiv.) at room temperature. (b) Kinetic study under different reaction conditions, including different temperatures and solvents. (c) Representative images of photoinitiated free-radical polymerization using the fully converted reaction mixture in a vial under red-light irradiation: (i) 10 μM after 20 min, (ii) 7.5 μM after 23 min, and (iii) 5 μM after 1 h, and (iv) 100 μM of (**2**) only after 1 h. The molar concentrations of (i)–(iii) were determined by the Beer–Lambert law using molar absorptivity of **CB**. The scale bar represents 1.5 cm.

and 23 min of the irradiation for 10 and 7.5 μM solution, respectively (Fig. 13c, i and ii). However, no hydrogel was observed for the 5 μM solution even after 1 h of irradiation (Fig. 13c, iii). As a negative control, 100 μM of (**2**) did not form a hydrogel after 1 h of irradiation (Fig. 13c, iv).

Furthermore, we investigated the polymerization kinetics of OEGMA using **CB** (**2**) before and after treatment with varying concentrations of TBAF. Specifically, TBAF was added at different concentrations to a solution of (**2**) (2 mM) in DMSO, followed by incubation at 37 °C for 5 min to facilitate the reaction. The resulting mixture was then mixed with an aqueous solution containing OEGMA (250 mM) and TEOA (200 mM) and adjusted to 50% DMSO (aq) under ambient conditions. Polymerization was initiated by the red-light irradiation for 6 h. The monomer conversion was considerably dependent on the

Open Access Article. Published on 09 March 2026. Downloaded on 3/10/2026 10:21:03 PM. This article is licensed under a Creative Commons Attribution-NonCommercial 3.0 Unported Licence.

concentration of TBAF. For example, monomer conversion increased to 82% at 0.2 mM TBAF, 34% at 0.1 mM TBAF and 8% at 0.05 mM TBAF (Fig. S42). In contrast, no monomer conversion was observed at 0.02 mM TBAF or in the absence of TBAF. These results indicate that a minimum TBAF concentration of approximately 0.1 mM is required to achieve polymerization of OEGMA within 6 h. Taken together, these results demonstrate the successful development of a switchable red-light photocatalyst/initiator based on sulfonyl-protected **CB**.

Conclusions

In summary, we developed a family of bridged fluorescein derivatives (**CB**, **BBF**, and **BEY**) that serve as efficient organic photocatalysts for red-light photoredox catalysis. To elucidate the underlying catalytic mechanism, we systematically investigated photoinitiated radical polymerizations, including photo-RAFT polymerization and free-radical photopolymerization. These polymerization investigations not only offer valuable mechanistic insights but also sever as versatile platforms for facile characterization of reactivity and various polymer-based applications. In particular, mechanistic investigations revealed that molecular oxygen plays a crucial role in facilitating photocatalysis as both an active redox mediator and a co-initiator. Additionally, incorporation of heavy halogen atoms into the bridged fluorescein backbone significantly enhances photocatalytic performance. This improvement is attributed to the heavy-atom effect, which increases intersystem crossing efficiency and highlights a rational design principle for tuning photocatalyst performance. Furthermore, development of a fluoride-responsive bridged fluorescein extends this concept to stimulus-responsive and light-controlled materials, opening new opportunities for applications in photodynamic therapy and cell surface engineering. Collectively, these findings establish bridged fluoresceins as a novel class of red-light photoredox catalysts and provide valuable mechanistic understanding and design principles for future photocatalyst development. Furthermore, we believe that this work will accelerate progress in biocompatible photochemistry, sustainable and wavelength-selective synthesis, and the development of stimulus-responsive functional systems.

Author contributions

The manuscript was written through contributions of all authors. All authors have given approval to the final version of the manuscript.

Conflicts of interest

There are no conflicts to declare.

Data availability

The data supporting this article have been included as part of the supplementary information (SI). Supplementary information: details of the materials, experimental procedures, characterization, and analytical and photophysical data. See DOI: https://doi.org/10.1039/d6sc01311b.

Acknowledgements

This research was supported by the National Research Foundation of Korea (NRF) (RS-2023-00239038).

Notes and references

1 D. Kim, J. You, D. H. Lee, H. Hong, D. Kim and Y. Park, *Science*, 2024, **386**, 99–105.
2 S. P. Pitre and L. E. Overman, *Chem. Rev.*, 2022, **122**, 1717–1751.
3 R. C. E. Silva, L. O. da Silva, A. D. Bartolomeu, T. J. Brocksom and K. T. de Oliveira, *Beilstein J. Org. Chem.*, 2020, **16**, 917–955.
4 D. M. Schultz and T. P. Yoon, *Science*, 2014, **343**, 985–994.
5 C. K. Prier, D. A. Rankic and D. W. C. MacMillan, *Chem. Rev.*, 2013, **113**, 5322–5363.
6 J. C. Theriot, C.-H. Lim, H. Yang, M. D. Ryan, C. B. Musgrave and G. M. Miyake, *Science*, 2016, **352**, 1082–1086.
7 W. Jin, C.-Y. Yang, R. Pau, Q. Wang, E. K. Tekelenburg, H.-Y. Wu, Z. Wu, S. Y. Jeong, F. Pitzalis, T. Liu, Q. He, Q. Li, J.-D. Huang, R. Kroon, M. Heeney, H. Y. Woo, A. Mura, A. Motta, A. Facchetti, M. Fahlman, M. A. Loi and S. Fabiano, *Nature*, 2024, **630**, 96–101.
8 J. Niu, D. J. Lunn, A. Pusuluri, J. I. Yoo, M. A. O'Malley, S. Mitragotri, H. T. Soh and C. J. Hawker, *Nat. Chem.*, 2017, **9**, 537–545.
9 C. Ash, M. Dubec, K. Donne and T. Bashford, *Laser Med. Sci.*, 2017, **32**, 1909–1918.
10 X. Li, Z. Zhang, B. Fan, Y. L. Li, D. J. Song and G. Y. Li, *Oxid. Med. Cell. Longev.*, 2022, 6881322.
11 X. He, S. Jin, X. Dai, L. Chen, L. Xiang and C. Zhang, *J. Clin. Med.*, 2023, **12**, 7488.
12 T. Zhang, S. Pradhan and S. Das, *Angew. Chem., Int. Ed.*, 2025, **64**, e202501194.
13 I. M. Irshadeen, V. X. Truong, H. Frisch and C. Barner-Kowollik, *Chem. Commun.*, 2022, **58**, 12975–12978.
14 B. D. Ravetz, A. B. Pun, E. M. Churchill, D. N. Congreve, T. Rovis and L. M. Campos, *Nature*, 2019, **565**, 343–346.
15 Z. Wu and C. Boyer, *Adv. Sci.*, 2023, **10**, 2304942.
16 A. H. Schade and L. Mei, *Org. Biomol. Chem.*, 2023, **21**, 2472–2485.
17 M. M. Hossain, A. C. Shaikh, R. Kaur and T. L. Gianetti, *J. Am. Chem. Soc.*, 2024, **146**, 7922–7930.
18 B. F. Buksh, S. D. Knutson, J. Oakley, N. B. Bissonnette, D. G. Oblinsky, M. P. Schwoerer, C. P. Seath, J. B. Geri, F. P. Rodriguez-Rivera, D. L. Parker, G. D. Scholes, A. Ploss and D. W. C. MacMillan, *J. Am. Chem. Soc.*, 2022, **144**, 6154–6162.
19 X. Hu, G. Szczepaniak, A. Lewandowska-Andralojc, J. Jeong, B. Li, H. Murata, R. Yin, A. M. Jazani, S. R. Das and K. Matyjaszewski, *J. Am. Chem. Soc.*, 2023, **145**, 24315–24327.

 © 2026 The Author(s). Published by the Royal Society of Chemistry

Open Access Article. Published on 09 March 2026. Downloaded on 3/10/2026 10:21:03 PM.
This article is licensed under a Creative Commons Attribution-NonCommercial 3.0 Unported Licence.

20 S. Dadashi-Silab, F. Lorandi, M. J. DiTucci, M. Sun, G. Szczepaniak, T. Liu and K. Matyjaszewski, *J. Am. Chem. Soc.*, 2021, **143**, 9630–9638.
21 R. Li, S. Zhang, X. Tang, G. G. Qiao, S. P. Armes and Z. An, *J. Am. Chem. Soc.*, 2025, **147**, 33153–33161.
22 A. Eftekhari, K. R. de Graaf, E. Takmakova, H. Jongprasitkul, A. Efimov, S. Turunen, A. Kerr, M. Kellomäki, R. Luxenhofer, T. Laaksonen and N. Durandin, *Adv. Mater.*, 2025, **37**, 2502386.
23 I. O. Levkovsky, L. Trachsel, H. Murata and K. Matyjaszewski, *Angew. Chem., Int. Ed.*, 2025, **64**, e202516164.
24 L. Trachsel, I. O. Levkovsky, X. Hu, H. Murata and K. Matyjaszewski, *J. Am. Chem. Soc.*, 2025, **147**, 32096–32109.
25 A. Aguirre-Soto, C.-H. Lim, A. T. Hwang, C. B. Musgrave and J. W. Stansbury, *J. Am. Chem. Soc.*, 2014, **136**, 7418–7427.
26 S. Kim and H. D. Sikes, *ACS Appl. Mater. Interfaces*, 2021, **13**, 57962–57970.
27 A. Aguirre-Soto, K. Kaastrup, S. Kim, K. Ugo-Beke and H. D. Sikes, *ACS Catal.*, 2018, **8**, 6394–6400.
28 D. P. Hari and B. König, *Chem. Commun.*, 2014, **50**, 6688–6699.
29 D. C. Neckers and O. M. Valdes-Aguilera, *Photochemistry of the xanthene dyes*, John-Wiley and Sons, 1993.
30 Y. J. Jung, H. Choi, I. S. Choi and J. K. Lee, *Chem. Commun.*, 2024, **61**, 322–325.
31 H. Kim, Y. J. Jung and J. K. Lee, *Polym. Chem.*, 2021, **12**, 970–974.
32 H. Ko, Y. J. Jung, M. Kim, H. Kim, D. Lee, R. Kim, W. O. Choi, H.-I. Lee and J. K. Lee, *Dyes Pigm.*, 2024, **226**, 112152.
33 J. B. Nganga, Y. J. Jung, Y. Si, M. Kim, H. Ko, G. T. Hwang, H. J. Lee, H.-I. Lee and J. K. Lee, *Dyes Pigm.*, 2022, **200**, 110163.
34 M. Tanioka, A. Kuromiya, R. Ueda, T. Obata, A. Muranaka, M. Uchiyama and S. Kamino, *Chem. Commun.*, 2022, **58**, 7825–7828.
35 M. Tanioka, M. Oyama, K. Nakajima, M. Mori, M. Harada, Y. Matsuya and S. Kamino, *Phys. Chem. Chem. Phys.*, 2024, **26**, 4474–4479.
36 C. Wu, N. Corrigan, C.-H. Lim, W. J. Liu, G. Miyake and C. Boyer, *Chem. Rev.*, 2022, **122**, 5476–5518.
37 C. F. Nising and S. Bräse, *Chem. Soc. Rev.*, 2008, **37**, 1218–1228.
38 J. Yoon, Y. J. Jung, J. B. Yoon, K. Damodar, H. Kim, M. Shin, M. Seo, D. W. Cho, J. T. Lee and J. K. Lee, *Polym. Chem.*, 2019, **10**, 5737–5742.
39 G. R. Fleming, A. W. E. Knight, J. M. Morris, R. J. S. Morrison and G. W. Robinson, *J. Am. Chem. Soc.*, 1977, **99**, 4306–4311.
40 F. L. Hatton, A. M. Park, Y. Zhang, G. D. Fuchs, C. K. Ober and S. P. Armes, *Polym. Chem.*, 2019, **10**, 194–200.
41 T. Rundlof, M. Mathiasson, S. Bekiroglu, B. Hakkarainen, T. Bowden and T. Arvidsson, *J. Pharm. Biomed. Anal.*, 2010, **52**, 645–651.
42 P. N. Kurek, A. J. Kloster, K. A. Weaver, R. Manahan, M. L. Allegrezza, N. D. A. Watuthanthrige, C. Boyer, J. A. Reeves and D. Konkolewicz, *Ind. Eng. Chem. Res.*, 2018, **57**, 4203–4213.
43 Y. Lee, C. Boyer and M. S. Kwon, *Chem. Soc. Rev.*, 2023, **52**, 3035–3097.
44 M. L. Allegrezza and D. Konkolewicz, *ACS Macro Lett.*, 2021, **10**, 433–446.
45 C. Stubbs, T. Congdon, J. Davis, D. Lester, S. J. Richards and M. I. Gibson, *Macromolecules*, 2019, **52**, 7603–7612.
46 A. Lerner, H. Kornweitz, I. Zilbermann, G. Yardeni, M. Saphier, R. Bar Ziv and D. Meyerstein, *Free Radic. Biol. Med.*, 2021, **162**, 555–560.
47 M. D. Thum, D. Hong, A. N. Zeppuhar and D. E. Falvey, *Photochem. Photobiol.*, 2021, **97**, 1335–1342.
48 D. H. Chin, G. Chiericato, E. J. Nanni and D. T. Sawyer, *J. Am. Chem. Soc.*, 1982, **104**, 1296–1299.
49 J. Sun, H. Zhao, S. Zhang, X. Xu, W. He, L. F. Zhang and Z. Cheng, *Macromolecules*, 2024, **57**, 756–765.
50 G. Ng, S. W. Prescott, A. Postma, G. Moad, C. J. Hawker and C. Boyer, *Macromol. Chem. Phys.*, 2023, **224**, 2300132.
51 J. Fan, C. Li, X. Guo and Y. Deng, *Polym. Chem.*, 2023, **14**, 773–783.
52 Y. Deng, C. Li, J. Fan and X. Guo, *Macromol. Rapid Commun.*, 2023, **44**, 2300258–2300264.
53 H. Bader, V. Sturzenegger and J. Hoigne, *Water Res.*, 1988, **22**, 1109–1115.
54 L. Zhang, C. Y. Wu, K. Jung, Y. H. Ng and C. Boyer, *Angew. Chem., Int. Ed.*, 2019, **58**, 16811–16814.
55 Y. Zhang, Y. Zhang, Y. Guo, S. Liu and X. Shen, *Chem Catal.*, 2022, **2**, 1380–1393.
56 X.-Z. Fan, J.-W. Rong, H.-L. Wu, Q. Zhou, H.-P. Deng, J. Da Tan, C.-W. Xue, L.-Z. Wu, H.-R. Tao and J. Wu, *Angew. Chem., Int. Ed.*, 2018, **57**, 8514–8518.
57 J. M. Yan, H. W. Cheo, W. K. Teo, X. C. Shi, H. Wu, S. B. Idres, L.-W. Deng and J. Wu, *J. Am. Chem. Soc.*, 2020, **142**, 11357–11362.
58 J. Wong, K. Kaastrup, A. Aguirre-Soto and H. D. Sikes, *Polymer*, 2015, **69**, 169–177.
59 A. Aguirre-Soto, S. Kim, K. Kaastrup and H. D. Sikes, *Polym. Chem.*, 2019, **10**, 926–937.
60 J. Kabatc, *J. Polym. Sci., Part A:Polym. Chem.*, 2017, **55**, 1575–1589.
61 C. G. Bailey, M. D. Nothling, L. L. Fillbrook, Y. Vo, J. E. Beves, D. R. McCamey and M. H. Stenzel, *Angew. Chem., Int. Ed.*, 2023, **62**, e202301678.
62 H. J. Avens and C. N. Bowman, *J. Polym. Sci., Part A:Polym. Chem.*, 2009, **47**, 6083–6094.
63 K. L. Willett and R. A. Hites, *J. Chem. Educ.*, 2000, **77**, 900–902.
64 G. Odian, *Principles of polymerization*, Wiley-Interscience, Hoboken, N.J, 4th edn, 2004.
65 H. Kim, D. Lee, Y. J. Jung, S. H. Yang, H. J. Lee, H.-I. Lee and J. K. Lee, *Chem. Sci.*, 2025, **16**, 15499–15509.
66 S. E. Braslavsky, *Pure Appl. Chem.*, 2007, **79**, 293–465.
67 M. A. Cismesia and T. P. Yoon, *Chem. Sci.*, 2015, **6**, 5426–5434.
68 E. E. Wegner and A. W. Adamson, *J. Am. Chem. Soc.*, 1966, **88**, 394–404.
69 S. Flynn, A. B. Dwyer, P. Chambon and S. Rannard, *Polym. Chem.*, 2019, **10**, 5103–5115.

Open Access Article. Published on 09 March 2026. Downloaded on 3/10/2026 10:21:03 PM.
This article is licensed under a Creative Commons Attribution-NonCommercial 3.0 Unported Licence.

70 N. A. Romero and D. A. Nicewicz, *Chem. Rev.*, 2016, **116**, 10075–10166.
71 D. Zhong, S. Liu, L. Yue, Z. Feng, H. Wang, P. Yang, B. Su, X. Yang, Y. Sun and G. Zhou, *Chem. Sci.*, 2024, **15**, 9112–9119.
72 H. J. Jiang, Z. Wang, B. Mao, Y. Bing, N. Sun and J. Yuan, *Spectrochim. Acta, Part A Mol. Biomol. Spectrosc.*, 2025, **325**, 125147.
73 W. O. Choi, Y. J. Jung, M. Kim, H. Kim, J. J. Li, H. Ko, H.-I. Lee, H. J. Lee and J. K. Lee, *ACS Omega*, 2023, **8**, 40277–40286.
74 P. Bilski, A. G. Belanger and C. F. Chignell, *Free Radic. Biol. Med.*, 2002, **33**, 938–946.
75 S. S. Eaton, G. R. Eaton and L. J. Berliner, *Biomedical EPR*, Kluwer Academic/Plenum Publishers, New York, 2004.
76 G. R. Eaton, S. S. Eaton, D. P. Barr and R. T. Weber, *Quantitative EPR*, Springer, Wien, New York, 2010.
77 M. Pinteala and S. Schlick, *Polym. Degrad. Stab.*, 2009, **94**, 1779–1787.
78 B. G. Magri, M. Barter, J. Fletcher-Charles, H. Choi, D. Slocombe, E. Richards, A. Folli, A. Porch and D. M. Murphy, *Res. Chem. Intermed.*, 2023, **49**, 289–305.
79 E. G. Janzen and J. I.-P. Liu, *J. Magn. Reson.*, 1973, **9**, 510–512.
80 Y. Zhou, J. F. Zhang and J. Yoon, *Chem. Rev.*, 2014, **114**, 5511–5571.
81 J.-W. Lee, M. T. Oliveira, H. B. Jang, S. Lee, D. Y. Chi, D. W. Kim and C. E. Song, *Chem. Soc. Rev.*, 2016, **45**, 4638–4650.
82 S. Kim and H. D. Sikes, *Polym. Chem.*, 2020, **11**, 1424–1444.

 © 2026 The Author(s). Published by the Royal Society of Chemistry